A Refined Morphodynamic Framework for the Inn River: Trajectories and Sediment Dynamics

Master Thesis

Dept. of Civil, Environmental, and Geomatic Engineering

July, 2025

Author
Yang He
Student ID 22-953-384

Supervisors
Ludovico Agostini
Prof. Dr. Peter Molnar

ETH zürich

Abstract

Rivers evolve under combined anthropogenic and natural influences across spatial and temporal scales, making morphodynamic prediction crucial for effective management. This study integrated historical evolutionary trajectories with sediment dynamics analysis to identify external drivers of river morphology and assess their impact on riverbed evolution. The approach was applied to the Inn River in the Engadine region, with a length of 58 km, which has undergone significant morphological changes due to multiple external factors.

The Inn River was segmented into 12 homogeneous sections, and reach-averaged morphological parameters from 16 aerial images (1946–2021) were analyzed for evolutionary trajectories. In the global view, discharge was identified as the dominant driver of active width trends, with widening–narrowing cycles corresponding to high–low flood events. Active width represents the zone shaped by water and sediment movement, while the centerline marks the central flow along the middle of the active width. Although connected to the active width, the centerline is also affected by asymmetric bank activities that can not be fully captured by reach-averaged metrics. In the sectional view, bar dynamics, channel braiding, and avulsion were strongly linked to the sediment supply, gravel extraction, and sediment transport. Disturbances in the sediment budget could activate channel morphodynamics, with effects persisting for several years.

Additional analysis of the river active width offered practical insights for river management. The relationship between average width and spatial variability in homogeneous sections provided a basis for estimating fluvially influenced zones. The relationship between active width variability and Taylor microscale identified areas that were more vulnerable or resilient to longitudinal disturbance propagation, allowing for precise evaluation of management impacts. While both active width and bottom width exhibited similar longitudinal trends due to shared geomorphic controls, active width was more sensitive to fluvial dynamics, whereas bottom width remained comparatively stable over time, suggesting that different driving forces governed changes in bottom width.

Sediment dynamics, represented by erosion and aggradation, were assessed using bedload transport rates derived from 1D hydraulic modeling (BASEMENT 4v) with eight sediment transport formulas. Discharge inputs were based on corrected PREVAH-simulated values that accounted for anthropogenic water redistribution. The model, which incorporated 26 tributaries, the Pradella derivation, and restitution at Martina, with the Pradella dam as an internal boundary, was run to a daily steady state. Results, based on 2010s discharge and channel geometry, were compared with measured bed elevation (η) changes for the periods 2000s–2010s and 2010s–2020s, integrated with channel bottom width (W_b), using the left side of the relation $\frac{d\eta}{dt}W_b = -\frac{dQ_b}{dx}$. The right term corresponded to modeled bedload transport gradients over distance (dQ_b/dx) between consecutive cross sections. For each cross section, these gradients from 10-year simulations were summarized as expected values, derived from probability density functions of results across all sediment transport formulas. Shear stress from daily PREVAH discharge was validated against hourly measurements, showing good overall agreement, with slight overestimation in the upstream sections and underestimation downstream. Comparison with observed bed changes indicated that the model effectively captured sediment dynamics in sections with sufficient sediment supply and limited external disturbances.

Contents

1 Introduction

Rivers continuously evolve across spatial and temporal scales under combined influences of anthropogenic activities (e.g. dam construction, sediment mining, urbanization) and natural drivers such as climate change. Prediction of river morphology is critical for efficient river management strategies, especially for the design and maintenance of water engineering structures and for ecological sustainability.

Given the inherent complexity of fluvial systems, historical evolutionary trajectories provide critical baselines for interpreting current conditions and forecasting future states, allowing engineers to set the most achievable management goals (Brierley and Fryirs (2009)). The concept of evolutionary trajectory emphasizes the response of river systems to past external influences and disturbance, thus defining a range of probable future conditions under different interventions. In river evolution, sediment transport dynamics play a fundamental role in shaping river morphology. Quantifying these processes, particularly the bedload transport, allows the reconstruction of historical channel changes and improves the predictive capacity for future trajectories (Church (2006)).

To fully capture the river behavior, a multi-perspective analytical approach is essential. At the catchment scale, rivers exhibit strong landscape connectivity, allowing the identification of key external forcings that influence fluvial processes. Zero-dimensional (0D) morphology analysis focuses on reach-averaged morphological parameters, such as channel width, centerline position, and other morphodynamic changes. This approach reveals long-term trends and the evolution of river reaches. Furthermore, one-dimensional (1D) hydrology analysis utilizes numerical modeling to simulate flow conditions and derive hydraulic variables, which are then used to estimate and assess bedload transport, erosion, and aggradation along the river. This integrated framework enables a comprehensive understanding of river dynamics.

Building on these concepts, this report investigated the morphodynamics of the River Inn in the Engadin Valley, Switzerland, which has experienced significant anthropogenic and natural influences over decades. The study was conducted in two steps:

- In the catchment scale, the river was segmented into homogeneous reaches using a methodological framework for hydromorphological assessment, analysis, and monitoring (IDRAIM) from Scorpio et al. (2017). 0D morphology analysis was conducted to reconstruct evolutionary trajectories over a 76-year period, enabling the identification of key drivers behind reach-scale morphodynamic changes.
- Based on 1D hydrology analysis, sediment transport dynamics were analyzed using a BASEMENT v4 numerical model (ETH Zurich, VAW (2024)). The bedload transport rates were then estimated to identify potential erosion and aggradation between the cross sections. The model outputs were validated against historical observations to assess the sediment dynamics and its influence on riverbed evolution.

By combining historical trajectory analysis with sediment transport estimation, this study showed the interplay between long-term channel change and sediment dynamics. The integrated approach enhances predictive capabilities for sustainable river management in the Alpine environment.

2 Study Area

The Inn River originates in the Swiss Alps, specifically west of St. Moritz in the Engadine region, at Piz Lunghin north of the Maloja Pass. From its alpine source, the Inn flows through Switzerland, Austria, and Germany, ultimately joining the Danube. In the Alpine region, the Inn has a length of 373 km and a catchment area of 20,234 km², making it the longest river in the Alps. (Egger et al. (2019))

This study focuses on the upper part of the Inn River from the Cinuos-chel gauge station to Martina, which is located in the Engadin Valley, Switzerland. The investigated river reach is 58.1 km long and drains a catchment area of approximately 1,161.4 km². As shown in Figure 2.1, the catchment encompasses portions of the Swiss National Park, providing a unique context of both protected and managed landscapes. The mean elevation of the area is around 2,400 m a.s.l. (BAFU, 2016). The Engadin Valley is classified as an inner-Alpine dry valley, characterized by a continental climate with pronounced seasonal temperature and precipitation variations (Abderhalden et al. (2016)). These climatic conditions, together with the elevation of the valley, influence the hydrological regimes in the study area.

Within the study area in Figure 2.1, four main tributaries, Spoel, Susasca, Clemgia, and Brancla, join the Inn from upstream to downstream. In addition, 22 smaller tributaries contributing to the river system has been identified, reflecting a complex and well-connected drainage network. The main channel exhibits an average slope of approximately 1%, indicative of a moderate gradient that supports both sediment transport and diverse channel morphologies (Church (2006)).

A significant anthropogenic feature in the study area is the presence of the Engadiner Kraftwerke AG (EKW) hydroelectric power company, which uses the water resources of the Inn and Spoel rivers for electricity generation. Within the study area, two major hydropower facilities indicated in Figure 2.1, are of particular relevance: the Pradella facility on the Inn River and the Ova Spin facility on the Spoel tributary, both commissioned in 1970. Each site includes a dam, a power plant, a balancing reservoir, and an interconnected network of water tunnels. This infrastructure enables regulation of water storage and release, allowing operators to optimize hydroelectric generation in response to fluctuating energy demands. Since the Ova Spin reservoir collects water from the natural catchment of the Spoel River, the part of the Spoel catchment upstream of the dam is excluded from the study area. The Ova Spin reservior also collects water from several derivations, including S-chanf, Vallember, Varusch and Clemgia, among others. The Pradella reservoir receives water directly from the Inn River and associated derivations. The water stored in these reservoirs is released back into the Inn River following certain operational rules at Martina. As a result, the flow regime in the study area has been altered from its natural state. (Engadiner Kraftwerke AG (2025))

Due to the ecomorphological impacts caused by the Ova Spin dam, a broad group of members of the Swiss National Park, the EKW, Federal, and Cantonal anthorities agreed to an experimental flood (e-flood) program starting in 2000. Since then, the controlled flood releases from the Ova Spin dam have been carried out regularly once or twice a year. The timing and magnitude of these releases vary, with peak discharges ranging from 15–25 to 20–40 m³/s, durations lasting 6–8 hours, and peak flows sustained for 2–3 hours. The primary aims of this program are to

enhance fish habitat, mobilize bed sediments, and restore channel morphology. (Robinson et al. (2018); Kevic et al. (2018); Hashemi et al. (2023))

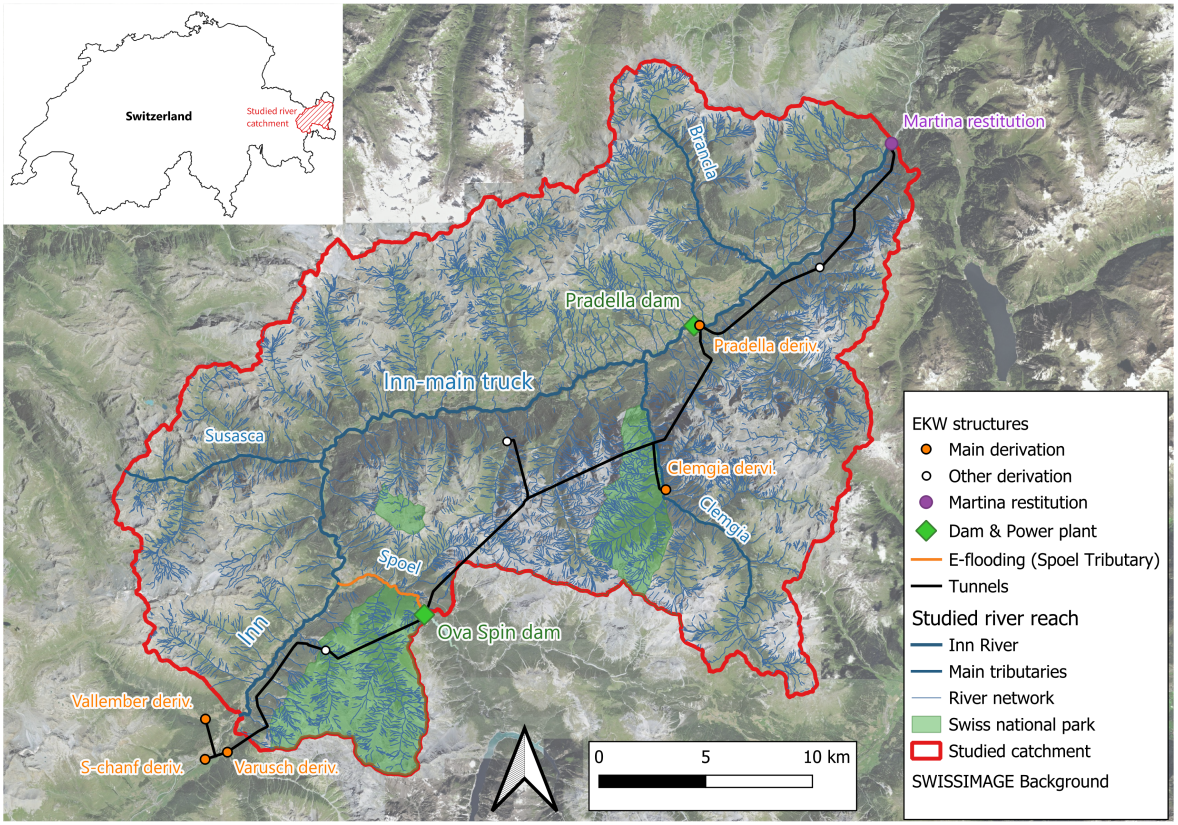

Figure 2.1: Study river reach and catchment overview with EKW infrastructure (flow direction: left to right).

Given its hydrological characteristics and management interventions, the Inn River reach provides an ideal setting to explore the interactions between natural processes and human activities in shaping riverbed evolution. This suitability is underscored by the following key factors:

- The river system has experienced a variety of anthropogenic interventions over several decades, including water redistribution and dam construction. These modifications enable the assessment of their impact on river morphology and sediment dynamics.
- The river is long enough for visualization of diverse morphodynamic patterns, from anthropogenically modified parts to naturally braided parts. This spatial variability enables the investigation of potential driving factors influencing fluvial process.
- The catchment exhibits a complex fluvial network, offering multiple potential sediment sources, which are essential to analyze sediment dynamics.
- There is a wealth of historical data, including aerial imagery, gravel extraction volumes, measured discharges, and river cross-sectional surveys over the past 20 to 76 years. This provides a solid foundation for temporal analyses of morphological changes.

3 Data Preparation and Description

3.1 Aerial Images

Aerial images provide views of the landscape photographed from aircraft. In this study, a series of aerial photographs covering the study area was obtained for 16 distinct years between 1946 and 2021, sourced from Federal Office of Topography swisstopo (2025). Detailed information for aerial images is presented in Table 3.1.

In Table 3.1, the ground resolution of these aerial imgaes ranges from 0.1 to 1 m. Prior to 1998, all available aerial images were captured in black and white. From 1998 onward, Swisstopo began providing color aerial images, initially through digital conversion of analog photographs and, since 2005, through direct digital acquisition. This progression in imaging technology ensures both the continuity and the increased quality of the data set used for temporal analyses of river morphology. (Swisstopo (2024a))

These aerial images are fundamental for identifying changes in river morphology, allowing analysis of active channel width, centerline migration, and other key morphodynamic processes. Furthermore, the temporal sequence of aerial images can facilitate the interpretation of the drivin forcings influencing the morphological evolution of the river throughout the study period.

Table 3.1: Summary of aerial images from Swisstopo

Name	Years	Ground Resolution	Color
SWISSIMAGE HIST 1946	1946	1 m	Grayscale
SWISSIMAGE HIST	1956, 1958, 1960, 1972 1977, 1984, 1990, 1996	0.5 m	Grayscale
SWISSIMAGE 50 cm	2002	0.5 m	RBG
SWISSIMAGE 25 cm	2005, 2008, 2011, 2014	0.25 m	RBG
SWISSIMAGE 10 cm	2018, 2021	0.1 m	RBG

3.2 River Cross-Sectional Profiles

Cross-sectional profiles of the river are systematically surveyed by the Swiss Federal Office for the Environment (FOEN/BAFU). As illustrated in Figure 3.1, the Inn River within the study area is divided into three distinct reaches, each surveyed individually. These surveys are typically conducted at approximately 10-year intervals over a period of 20 years, with cross sections spaced at an average distance of 150 m (see Table 3.2). In total, 350 cross sections have been measured along the study river reach. For the purposes of analysis, cross-sectional measurements collected between 2009 and 2016 are grouped to represent the river geometry during the 2010s. Similarly, data from 2000–2006 and 2019–2021 are categorized as representing the “2000s” and “2020s,” respectively.For sections intersecting bridges, the geometry of bridge piers is also documented to facilitate more accurate hydraulic analysis.

For each cross section surveyed, the riverbed bottom is delineated and its mean elevation is calculated (see Appendix A.1 for calculation details). The riverbed bottom is defined as the

portion of the cross-sectional profile subject to sediment transport, erosion, and deposition. It is determined based on a combination of vegetation boundaries, substrate characteristics, and channel geometry, following the technical guidelines outlined in Ufficio federale dell'ambiente (FOEN/BAFU) (2017).The width of the riverbed bottom, together with changes in mean bottom elevation, can be used to calculate the volume of erosion and deposition.

In the study area, one unmeasured reach of cross sections was identified in Figure 3.1. To address this, 48 river cross sections were extracted from the most recent high-resolution Digital Elevation Model (DEM), SwissAlti3D in 2019, provided by Swisstopo (2024b). Corrections were applied to account for water surface elevation, as detailed in Appendix A.2.

These cross-sectional datasets are essential for detecting morphological changes such as channel erosion and aggradation. In addition, they provide critical input for numerical modeling of Inn River.

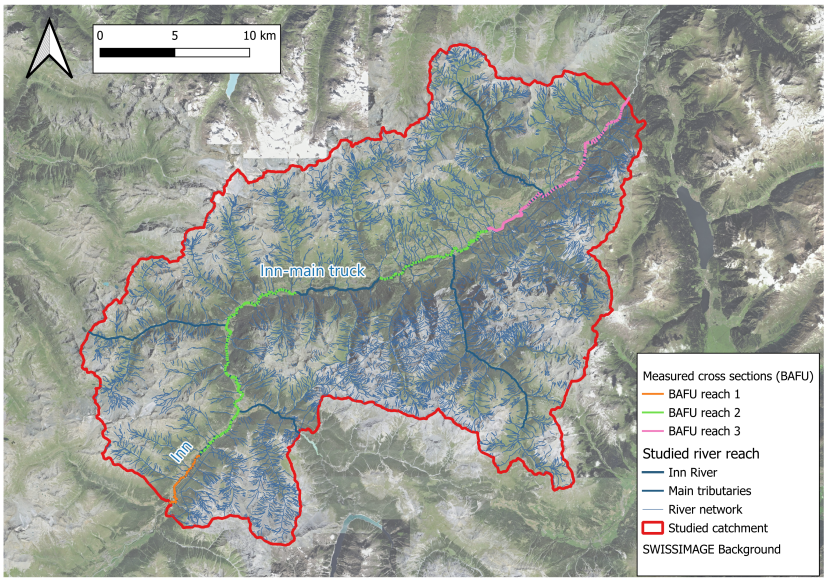

Figure 3.1: Measured cross-sectional data from bafu (350 cross sections in total) with one unmeasured reach

Table 3.2: Summary of measured cross-sectional data from BAFU

Reach	Location	Distance (km)	Years		
			2000s	2010s	2020s
1	Cinuos-chel - Brail	0 – 4.987	2006	2016	\
2	Brail - Pradella	5.098 – 24.482 31.607 – 41.589	2002	2011	2021
3	Pradella - Martina	41.791 – 58.051	2000	2009	2019

3.3 Discharge

Discharge is a key driver of river morphology, reflecting overall flow conditions and flooding periods and intensity, and serving as a critical input for numerical modeling. In this study,

measured discharge data from the BAFU gauging station and EKW diversion and restitution points were analyzed, complemented by simulated discharge values through hydrological model. The location of the BAFU gauging stations and EKW infrastructures can be seen in Figure 3.2.

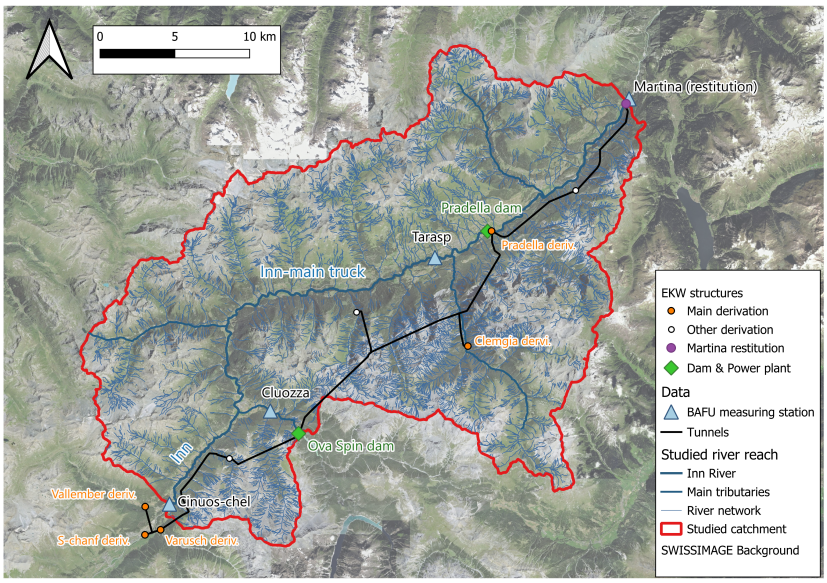

Figure 3.2: Discharge gauging stations from BAFU and EKW operational discharge data.

3.3.1 Measured Discharge - BAFU

In Figure 3.2, there are three BAFU gauging stations located along the Inn River within the study reach: Cinuos-chel, Tarasp, and Martina, arranged from upstream to downstream. The Cinuos-chel and Martina stations also delineate the upstream and downstream boundaries of the study area, respectively. Additionally, the Ova da Cluozza-Zernez (Cluozza) station, located at the confluence of the Ova da Cluozza tributary, measures the discharge contributed by this tributary to the Spoel River, which subsequently flows into the Inn. A summary of the BAFU-measured discharge is presented in Table 3.3.

Table 3.3: Summary of measured discharge (m^3/s) from BAFU station

BAFU station	Location	Period of record	Resolution
Cinuos-chel	Inn	1975-01-01 to 2023-12-31	1 hour
Cluozza	Ova da Cluozza	1974-01-01 to 2024-05-17	5 min
Tarasp	Inn	1975-01-01 to 2023-12-31	1 hour
Martina	Inn	1975-01-01 to 2023-12-31	1 hour

3.3.2 Operational Discharge Data - EKW

A total of eight water derivations and one restitution are associated with the Inn River, situated on both the main stem and its tributaries (Figure 3.2). For simplification, only derivations with a maximum capacity greater than 1.5 m^3/s are considered; smaller derivations are grouped as "other derivations" in Figure 3.2. Data for the Vallember and Varusch derivations are not available. A comprehensive overview of the available EKW operational data is presented in Table 3.4.

Table 3.4: Summary of EKW operational discharge data (m^3/s)

EKW infra.	Location	Period of record	Resolution	Max. capacity (m^3/s)
S-chanf deriv.	Inn	2018-01-01 to 2024-05-01	1 min	40
Vallember deriv.	Vallember	/	/	5
Varusch deriv.	Ova da Varusch	/	/	5.2
Clemgia deriv.	Clemgia	2018-01-01 to 2024-05-01	1 min	8
Pradella deriv,	Inn	2018-01-01 to 2024-05-01	1 min	20
Martina restit.	Inn	2016-01-30 to 2025-04-17	1 hour	/

3.3.3 Simulated Discharge - PREVAH Model

Runoff in the study area was simulated using the spatially distributed hydrological model PREVAH (Precipitation-Runoff-Evapotranspiration HRU Model). For the simulation, the catchment was subdivided into hydrological response units (HRUs) based on topographic characteristics and soil properties. Meteorological data were then incorporated to simulate the hydrological response of each HRU. The runoff generated by each HRU was then aggregated to obtain the total runoff for the specific catchment, which was routed to the Inn River as discharge. (Viviroli et al. (2009)) This modeling approach provided simulated daily discharge data at 27 locations along the Inn River, from S-chanf to Martina, covering the period from 1981-01-01 to 2022-12-31.

PREVAH simulated natural hydrological conditions and did not incorporate anthropogenic influences such as water management or hydropower operations (e.g., EKW). As a result, the effects of water extraction, redistribution, and restitution by hydropower facilities were not included in the initial simulations. Since the PREVAH-simulated discharge served as input for subsequent modeling, it was necessary to correct the PREVAH-simulated discharge values to account for the EKW operations, ensuring a realistic representation of actual river conditions.

3.3.4 Corrected Simulated Discharge Incorporating EKW Operations - PREVAH Model

To correct the PREVAH-simulated discharge for anthropogenic influences, it was necessary to derive water redistribution rules for the EKW infrastructure based on operational data (see Table 3.4). For the water derivations, linear relationships up to their maximum capacity were established by comparing the corresponding PREVAH-simulated discharge at each intake location with the actual water derivation data over the available time period. This approach allowed the estimation of the proportion of water diverted into the water tunnel under natural conditions. For the Vallember and Varusch derivations, where operational data were unavailable, it was assumed that their diversion behavior followed the same linear relationship as the Clemgia derivation. This assumption can be justified by their similar capacities and locations, as both have a maximum capacity under 10 m^3/s and are situated on tributaries.

Within the Spoel tributary, it was assumed that only the discharge from Ova da Cluozza reaches the Inn River, as water from the natural Spoel catchment is extracted by the Ova Spin hydropower facility.

For the Martina restitution, a yearly pattern of mean daily water returns was developed using the available restitution data listed in Table 3.4. To account for natural variability, daily restitution

discharges were randomly sampled within the standard deviation calculated from seven years of data. The water restitution regime at Martina changed in 1993 due to the construction of the Pradella dam. Therefore, the sampled annual pattern is representative only for the period from 1994 onward.

Using the derived EKW operational rules, the PREVAH-simulated discharge was corrected and subsequently validated against BAFU-measured discharge data at the Cinuos-chel, Tarasp, and Martina gauging stations. For consistency, the BAFU data was converted to daily resolution. The comparison results, including Nash–Sutcliffe efficiency (NSE) and mean error metrics (see Appendix A.3 details of metrics), are presented in Table 3.5.

Table 3.5: Comparison of BAFU-simulated discharge with PREVAH-simulated discharge after incorporating EKW operations

Location		Cluozza	Cinuos-chel	Tarasp	Martina
Time period		1981 - 2022	1981 - 2022	1981 - 2022	1994 - 2022
Metrics	NSE	0.74	0.577	0.859	0.715
	Mean error	10.03%	23.87%	-7.19%	3.91%

Table 3.5 presents the model evaluation at the Cluozza BAFU gauging station, which is unaffected by anthropogenic influences. A comparison between PREVAH-simulated and BAFU-measured discharge on the Ova da Cluozza tributary was performed at daily resolution from 1981 to 2022. The model showed good performance, with a Nash-Sutcliffe Efficiency (NSE) of 0.74 and a mean error of 10.03%, indicating a consistent overestimation. This may result from unaccounted natural losses such as infiltration or evaporation.

Based on Figure 3.2, the Cinuos-chel gauging station is influenced by three water derivations: S-chanf, Vallember, and Varusch. Further downstream, the Tarasp gauging station is additionally affected by the Ova Spin dam, which limits the discharge entering the Inn River from the Spoel tributary. At the most downstream station, Martina, the gauged discharge reflects not only the cumulative impact of all upstream EKW operations affecting Tarasp but is also influenced by the Pradella, Clemgia derivation, and the Martina restitution.

At the Cinuos-chel station, the validation results are less satisfactory, with an NSE of 0.577 and a mean error of 23.87% showing in Table 3.5. This reduced performance is likely due to the simplification of water derivation rules for the three major upstream derivations (S-chanf, Vallember, and Varusch), which together have a maximum capacity of 50.2 m^3/s. The assumption of a linear relationship between incoming flow and water extraction may not accurately capture the complex operational patterns, potentially leading to an underestimation of discharge extracted. Additionally, unaccounted anthropogenic influences upstream of S-chanf may further distort the simulated results.

At Tarasp station, the model performs well, with an NSE of 0.859 and a mean error of -7.19% as Table 3.5. The negative mean error value suggests a slight underestimation of discharge, possibly due to an overestimation of water extraction from the Spoel catchment by the Ova Spin hydropower facility. E-floods events mentioned in section 2 for river restoration, which have occurred since 2000, were not included in the discharge correction and may contribute to this discrepancy.

For Martina, the model shows good agreement with observations, with a mean error of 3.91% over a 29-year period, which is comparable to the model's performance under natural conditions at Cluozza over 41 years, as shown in Table 3.5.

Overall, while the discharge performance at Cinuos-chel is less satisfactory, its impact is mitigated downstream as natural flows are progressively aggregated. The results at Tarasp and Martina stations demonstrate that the corrected PREVAH-simulated discharge reliably represents actual river conditions, with Tarasp serving as a mid-reach validation point and Martina reflecting the outflow of the study area.

Comprehensive details of the EKW water redistribution rules and all validation figures are provided in Appendix A.4. In addition to the goodness-of-fit analysis using NSE and mean error, residual analysis was also employed to validate the modified PREVAH-simulated discharge. A comparison of the goodness-of-fit metrics and residual analysis results is also provided in Appendix A.4.

3.4 Grain Size Distribution

The grain size distribution (GSD) along the Inn River and its tributary, the Spoel, was investigated at selected locations using both surface and subsurface sampling methods. Surface sediment samples were collected using the Wolman pebble count technique (Wolman (1954)), while subsurface samples were analyzed by standard sieving procedures. The sampling locations are indicated in Figure 3.3.

The GSD data were utilized in bedload transport rate calculation after numerical modeling, with a particular analysis on average depositional/aggradational trends. So a combined GSD was derived from both surface and subsurface samples, following the flexible combination method presented by Anastasi (1984). Figure 3.4 presents the characteristic percentiles (10th, 25th, 50th, 75th, and 90th) of the combined GSD using boxplots. Pradella Dam is situated between the Ardez and Ramosch sampling locations. Detailed information on both surface and subsurface GSDs is provided in Appendix A.5.

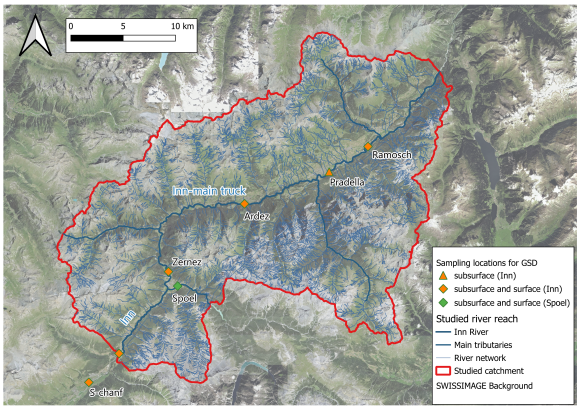

Figure 3.3: Locations for surface and subsurface sampling for GSD

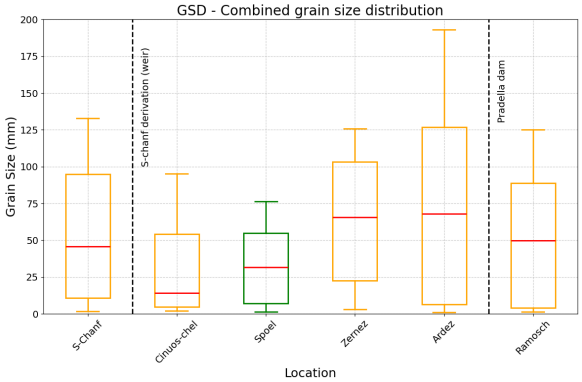

Figure 3.4: Combined GSD and infrastructure effects on sediment transport.

Based on Figure 3.4, the S-chanf sampling site is located upstream of the EKW water diversion

facility, where a weir raises the Inn River by approximately six meters to facilitate water extractionEngadiner Kraftwerke AG (2025). This backwater effect reduces flow velocity and the river's capacity to transport sediment, particularly coarse material, thereby limiting gravel supply to downstream reaches. The Vallember and Varusch tributaries, situated between Cinuos-chel and S-chanf, have low mean daily discharges (less than 2 m^3/s according to PREVAH simulation) and primarily contribute fine sediments. Consequently, the GSD at Cinuos-chel indicates a fining trend, driven by limited gravel input and continued supply of fine sediment from these low-discharge tributaries.

Downstream of Cinuos-chel, the GSD at the Zernez sampling location becomes coarser. This coarsening can be attributed to six debris flows that occur between Cinuos-chel and Zernez, delivering substantial amounts of coarse sediment to the river. Additionally, the main tributary Spoel enters the Inn upstream of Zernez. Although the GSD data for the Spoel (see Figure 3.4) suggest that it does not contribute significant coarse sediment, its inflow likely increases the river's transport capacity in the Inn River, facilitating the downstream movement of finer sediments. This enhanced transport of fine material may leave behind a relatively coarser bed at the Zernez location. The largest gravel mining site in the study area (see Section 3.5) is upstream of the sampling site of Zernez, which could influence the GSD downstream. It is possible that the site extracted fine and intermediate sediment, resulting in a coarser GSD at the downstream site of Zernez.

The Ardez sampling location exhibits a wider range of combined GSD, which can be attributed to the marked contrast between surface and subsurface GSD. As shown in Appendix A.5, the surface GSD at Ardez is notably coarser, indicating that fine grains have been selectively transported away, likely a result of the area's high flow intensity (see Figure 5.7). This strong transport capacity removes finer sediments and leaves behind a coarse surface layer. In contrast, the subsurface GSD is finer, reflecting the presence of historical fine sediment deposits. The armoring process in the surface layer also protects the finer subsurface sediment from being transported away. Overall, the GSD at Ardez is influenced more by local sediment supply and hydraulic conditions than by the general upstream–downstream fining or coarsening trends Massong and Montgomery (1999), resulting in significant variability between surface and subsurface GSD and a broader overall range of grain sizes at this site.

The Ramosch sampling location is situated downstream of the Pradella dam. In this reach, bed armoring is expected due to a sediment deficit caused by the dam, which blocks the downstream transport of coarse material. Over time, the lack of sediment replenishment leads to gradual removal of finer particles by the river, resulting in a coarser subsurface sediment layer. Upstream of the Pradella dam, only subsurface samples were collected at the Pradella site, as shown in Figure 3.3. The subsurface GSD data between Pradella and Ramosch (see Appendix A.5) show a slight downstream coarsening trend, supporting the hypothesis of incipient bed armoring below the dam.

The combined GSDs at S-chanf and Ramosch are remarkably similar in Figure 3.4, despite the roughly 40 km distance between these sites. This observation suggests that both sites receive sediment inputs with comparable grain size characteristics, likely due to similar contributions from debris flows and tributary inflows within the catchment. Such uniformity in sediment supply mechanisms across the basin may result in the convergence of GSD profiles at these otherwise geographically distinct sampling locations.

3.5 Gravel-mining Sites

Instream gravel mining involves the mechanical removal of gravel and sand directly from the channels of rivers and streams, serving as a significant driver of sediment dynamics and river geomorphology (Kondolf (1994)).

In Figure 3.5, there are five gravel-mining sites situated along the Inn River and its tributaries, with only two sites on the Inn River currently active. According to data from the Tiefbauamt Graubünden (Civil Engineering Office of Graubünden), the total volume of approved gravel extractions from water bodies within the study catchment amounts to 2,265,174 m^3 between 1949 and 2023. This dataset includes annual records of extraction volumes and specific locations, as detailed in Table 3.6. Among these, the Zernez site has the longest operational period and the largest cumulative extraction volume of 1,373,457 m^3.

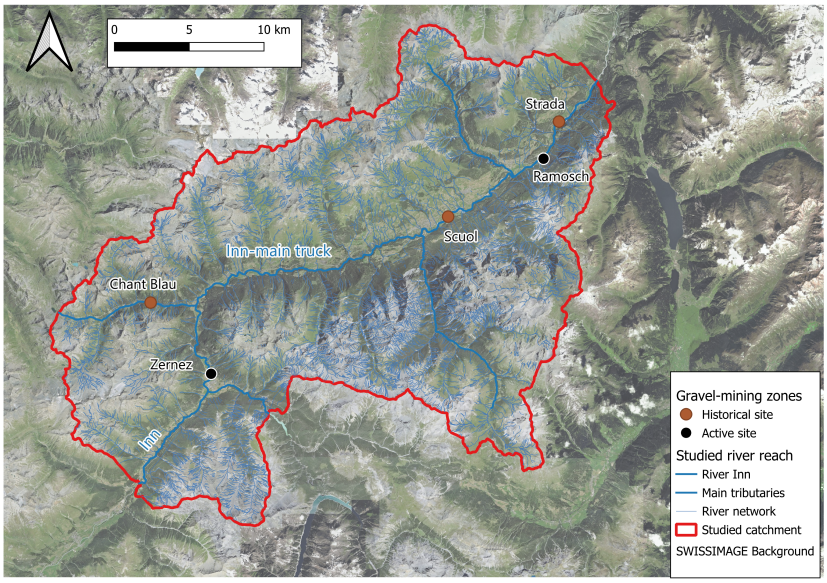

Figure 3.5: Locations of gravel-mining sites in the study area

Table 3.6: Summary of gravel-mining data in study area

Location	River	Time Period	Status	Number of Years	Avg. Annual Volume (m^3/yr)
Zernez	Inn	1962 – 2023	Active	62	22,152.53
Chant Blau	Susasca	1985 – 2003	Inactive	17	4,093
Scuol	Inn	2019 - 2022	Inactive	4	8,530.75
Ramosch	Inn	1966 – 2023	Active	58	9,238.60
Strada	Inn	1965 – 1994	Inactive	28	9,336.18

4 Method

4.1 Evolutionary Trajectories

4.1.1 River Characterization and Segmentation

The study Inn river was analyzed in the catchment scale and separated into homogeneous spatial units based on their distinct characteristics (Rinaldi et al. (2015)). The segmentation criteria included lithology, riverbed slope, channel confinement, sediment sources and sinks, and channel morphology. Detailed criteria and corresponding data sources are presented in Table 4.1, with the analysis proceeding sequentially from top to bottom as shown in the table.

Table 4.1: Criteria for the river segmentation based on characteristics

Characteristics	Description
Lithology	Sedimentary rock, metamorphic rock, volcanic rock.
Riverbed Slope	Median riverbed slope calculated between consecutive cross-sections.
Lateral Confinement	- Moderately confined (overflow possible)
	- Human confined (with levees or embankments)
	- Valley confined (limited by topography)
Sediment Sources/Sinks	Sources: Tributaries, debris flow
	Sinks: Dams, gravel-mining zones
Planimetric Morphology	Single Thread:
	- Straight (sinuosity 1.0-1.1)
	- Sinuous (sinuosity 1.1-1.5)
	- Meandering (sinuosity >1.5)
	Multi-Thread:
	- Anabranching (multiple channels with persistant vegetated islands)
	- Braiding (multiple channels without vegetated islands)
	- Wandering (transitional state between meandering and braiding)
Altimetric Morphology	Plane bed; Point and alternate bars

The data sources utilized for this analysis were as follows: Lithology information was obtained from lithological maps provided by Swisstopo.The riverbed slope was calculated using cross-sectional profiles from the 2010s, based on both BAFU measurements and DEM-derived data (see Section 3.2). Channel confinement was assessed using the ecomorphological classification of river reaches from BAFU, combined with digital elevation models from Swisstopo. Channel morphology and other related characteristics were evaluated through the interpretation of aerial imagery (see Section 3.1). The river characterization and segmentation were based on the most recent available data reflecting current conditions of the Inn River.

Tributaries and debris flows were differentiated at confluences by examining sediment and flow characteristics. Tributaries were recognized where the incoming flow was clear and lacked significant debris deposits at the confluence. In contrast, debris flows were identified at confluences characterized by substantial sediment accumulation.

4.1.2 River Active Width and Centerline

The morphological parameters of river active width changes and centerline migration were utilized for 0D analysis within each river section separated in Section 4.1.1. Active width is defined as the river and its adjacent areas that are actively shaped and modified by the movement of water and sediment over time, while centerline refers to the central flow path running along the middle of the active width. Temporal changes in both the active width and centerline position were evaluated using available aerial imagery, as described in Section 3.1. The analysis included 16 distinct years from 1946 to 2021.

The active channel width was manually delineated from aerial imagery, primarily following the vegetation edges on both riverbanks. Vegetated bank areas were assumed to be relatively stable and less affected by fluvial disturbance or morphological changes. The digitized banklines were then processed using the MATLAB code from Redolfi et al. (2016), which applies a moving-average filter and spline interpolation to refine the geometry. Based on the smoothed banklines, cross-sections perpendicular to the left and right banks were automatically extracted at 10 m intervals using the geometric intersection method. The middle point of the extracted crosss-sectional data were used as the river centerline.

Considering the limited resolution of the aerial images and the bankline smoothing, the positional uncertainty needed to be taken into account. For simplification, the hand-drawn error was ignored. Detailed analysis is shown in Appendix A.6.

Evolutionary Trajectory for River Active Width Changes

For the 0D morphological analysis, the reach-averaged active width was calculated using a weighted mean together with the semi-interpercentile range (half of the 16th–84th percentile range) to represent variability. Initially, a direct comparison between 1946 and 2021, the first and last years of the study period, was conducted to provide an overview of active width changes and their associated variability for each river section.

To reconstruct the evolutionary trajectory of the river's active width from 1946 to 2021, the reach-averaged active width for each year was normalized relative to its 1946 value. The normalization was computed as Equation (4.1).

$$\text{Normalized Active Width} = \frac{W_t}{W_{1946}} - 1 \tag{4.1}$$

where W_t is the active width at year t (m), and W_{1946} is the reference width from 1946 (m).

Similarly, the associated variability band was scaled using Equation (4.2).

$$\text{Scaled Variability Band} = \frac{\Delta W_t}{W_{1946}} \tag{4.2}$$

where ΔW_t denotes the variability in active width at year t (m).

This approach enables the visualization of active width change trend for each river section across 16 distinct years between 1946 and 2021. The difference in normalized active width between consecutive surveyed years was analyzed to detect periods of widening, narrowing, or stability for each river section. Uncertainties related to image resolution and bankline smoothing were rigorously propagated and incorporated into the analysis, following the procedures detailed

in Appendix A.6. Based on the magnitude of the normalized width difference relative to its propagated uncertainty, three categories were defined:

- Narrowing period: the two consecutive measured years showed a reach-averaged active width decreasing, and the magnitude is larger than the uncertainty.
- Widening period: the two consecutive measured years showed a reach-averaged active width increasing and the magnitude is larger than the uncertainty.
- Stable period: the two consecutive measured years showed reach-averaged active width relative changes within the uncertainty range.

Evolutionary trajectory for River Centerline Migration

For the 0D morphology analysis for the centerline, the migration rate for each sectional reach was calculated. For two centerlines from two consecutive years surveyed, the formulas are as in Equation (4.3).

$$\text{Migration Rate (m/yr)} = \frac{A_s}{L_{\text{avg}} \cdot \Delta T} \tag{4.3}$$

where A_s represents the shaded area between two centerlines from consecutive surveyed years (m^2), L_{avg} is the average length of the two centerlines (m), and ΔT is the time difference between the two survey years (yr). In particular, the intensity of the centerline migration was analyzed without considering the direction of migration.

To reconstruct the evolutionary trajectory of centerline migration rates, the mean migration rate for each section over the period 1946–2021 was first calculated and used as a reference value. Subsequently, the migration rates for each time interval were normalized by dividing by the respective section's mean migration rate. The standard deviation of these normalized migration rates was then computed to quantify temporal variability. Based on the relationship between the normalized migration rates and their standard deviation (*std.*), three temporal states were defined:

- Active period: the normalized centerline migration is larger than 1 + *std.*
- Inactive period: the normalized centerline migration is in between the 1-*std.* and 1+*std.*
- Unchanged period: the normalized centerline migration is smaller than 1-*std.*

Uncertainties related to image resolution and bankline smoothing were not considered in the centerline migration analysis, as these uncertainties are inherent in both the normalized migration rates and the calculated standard deviation.

4.1.3 Other Morphological Processes

In addition to analyzing changes in the river's active width and centerline, a range of other morphological processes occurring within the study reach were investigated using aerial images, as described in Section 3.1. These processes include:

- Retreat of vegetation bars: Reduction in vegetated bar area, assuming vegetation grows unless disturbed.

- Alternate bars dynamics: Formation/expansion, disappearance, and migration of alternate bars.
- Emergence/Disappearance of braided reaches: The formation or disappearance of braided channel parts within the river reach.
- Avulsion of channel path: Shifts in the river main flow path.

These morphological processes were systematically summarized and analyzed within the defined segmented river sections.

4.1.4 Analysis of External Forcings

Based on the study area characteristics and the available datasets, several potential external drivers of fluvial morphodynamics were identified. These include gravel mining activities, debris flows and tributary inputs, dam construction and operation, e-flooding in the Spoel tributary, and natural floods. The analysis of these driving forcings was conducted from two complementary perspectives: a global view of the entire river reach, and a sectional view focused on 12 defined river sections.

Gravel-mining sites and activities were documented using records described in Section 3.5. Debris flows and tributary inputs were identified and summarized through analysis of aerial images; it was assumed that a debris flow or tributary was active in the year of its first clear appearance in the corresponding imagery. Dam-related disturbances originate from the Ova Spin dam (in operation since 1968) and the Pradella dam (since 1993), both constructed and managed by the EKW company. E-flooding of the Spoel tributary have occurred once or twice annually since 2000.

Flooding represents a fundamental driver of channel morphology. Accordingly, both the duration and intensity of flooding events were quantified using both corrected PREVAH-simulated discharge data and BAFU-measured discharge data, as described in Section 3.3.

- Duration: The total number of flood days within a year.
- Intensity: The maximum discharge or unit discharge (discharge per meter of channel width) recorded within a flooding year.

BAFU-measured discharge data provided a comprehensive overview of river flow conditions across the main Inn River. Flooding durations were defined as days when discharge values exceeded the 99th percentile at all three gauging stations in the Inn River (Cinuos-chel, Tarasp, and Martina). For each year with flood events, the maximum recorded discharge was used to represent flood intensity. The maximum discharge for each flooding year from the upstream The flood intensity at the Cinuos-chel station was selected as the representative flood value for the entire river. This selection was validated by comparing across all three stations and confirmed by the similarity in rankings of flood intensity across flooding years (see Appendix A.7).

To obtain section-specific flow characteristics, PREVAH-simulated discharges were employed and analyzed at the scale of each river section. For each section, the outflow discharge was used to characterize flow conditions for each river section. Since PREVAH data are available at daily resolution, flood events were defined as days with discharge exceeding the 90th percentile for each section. Annual flood duration and flood intensity were calculated accordingly. To

enable meaningful comparison between river sections, the outflow discharge was normalized by the active channel width extracted from the year closest to the discharge measurement. This produced a unit discharge (discharge per meter of channel width), allowing flow intensity to be compared across the river sections.

In summary, these five potential driving forcings provide both global and sectional perspectives on the factors influencing river morphology and sediment transport within the study reach.

4.1.5 Further Analyses of River Active Width

Relationship Between Weighted Mean and Variability of River Active Width

For each section and survey year, it had both the weighted mean and the variability (half of the 16th–84th percentile range). The weighted mean values were plotted against their corresponding variability values to estimate their relationship. To establish a linear relationship between mean and variability, data pairs from sections 10 and 11 were excluded from the analysis.

Scaling Relationship Between Active Width Variability and Taylor Microscale

For each river reach and survey year, the spatial series of active width measurements was analyzed using autocorrelation to compute the autocorrelation function (ACF). The ACF was fitted with either a Gaussian or exponential model, both normalized to have a peak value of 1 at zero lag. The selection was based on minimization of the mean error between the ACF and the fitted distribution across the first four lag distances. If the Gaussian model provided the better fit, a parabolic approximation was constructed by matching the first and second derivatives of the Gaussian ACF at zero lag. Alternatively, if the exponential model fit better, a linear approximation was derived by matching the first derivative of the exponential ACF at zero lag. The intersection of these approximating functions (parabola or line) with the abscissa defined the Taylor microscale, which characterized the spatial scale over which fluctuations in river active width remained correlated before smaller-scale variability became dominant.

The variability values from each river reach and survey year was plotted against the corresponding Taylor microscale values obtained from the autocorrelation analysis on a log-log scale to investigate their scaling relationship.

Comparison of River Active Width and Bottom Width

The riverbed bottom width values, as described in Section 3.2, were provided by the BAFU. These measurements represent the river width subject to sediment transport, erosion, and deposition processes in the riverbed. To validate the hand-drawn active width data, the measured bottom width values were first compared with the active width values from the nearest corresponding years along the river to assess whether both datasets exhibit similar spatial variability.

Subsequently, the bottom width values were grouped by river section, and mean values were calculated for each section. To enable a temporal comparison of changes over time, the bottom width values were normalized relative to the 1946 active width baseline, as described in Equation (4.1). This normalization allowed direct comparison of temporal trends in bottom width and active width across the years.

4.2 Sediment Dynamics

After analysis of river morphology in the 0D perspective, 1D morphology analysis was based on the numerical modelling and bedload transport calculation to analyze the riverbed erosion and aggradation between cross sections. The estimated bedload changes were compared with measured data to localize the potential driving forcings.

4.2.1 Rationale for 1D Hydrological Analysis

Riverbed changes occur at various spatial scales, with smaller-scale bed level changes generally happening more rapidly than those at wider spatial extents (Van Denderen et al. (2022)). Compared to river active width and centerline dynamics, for which data is available for over 70 years, riverbed elevation data is only available for the 20-year period from the 2000s to the 2020s. Within this relatively short timeframe, observed riverbed changes are highly localized and are closely linked to site-specific natural events or human interventions.

For example, Figure 4.1 shows the longitudinal profile of the riverbed in section 5, measured every 10 years along with the corresponding driving forcings. Under the assumption of a continuous riverbed, any abrupt changes in bed elevation may indicate the influence of specific external drivers. The figure demonstrates that riverbed elevation changes are concentrated at sites affected by gravel mining. However, when calculating reach-averaged metrics such as mean bed elevation and overall channel slope, these localized changes are smoothed out, making it difficult to accurately identify the underlying causes of change. Consequently, a cross-sectional analysis based on numerical modeling is essential for a comprehensive assessment of riverbed morphological evolution.

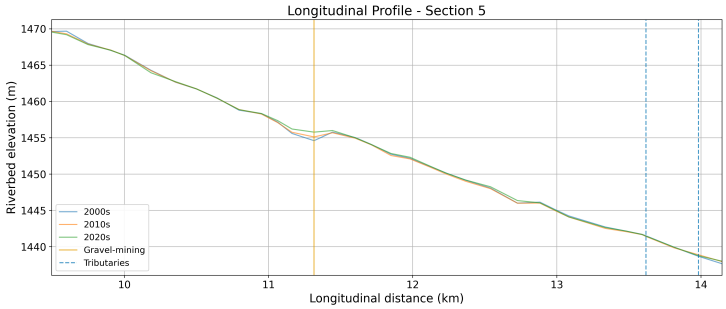

Figure 4.1: Longitudinal riverbed profile in section 5 with potential driving forcings (2000s–2020s)

4.2.2 1D Hydraulic Model Setup and Simulation

The 1D hydraulic modeling for this study was conducted using the BASEMENT 4v software environment (ETH Zurich, VAW (2024)). The model geometry was built using cross-sectional data measured in the 2010s (as detailed in Table 3.2) and supplemented with additional cross sections extracted from the 2019 DEM mentioned in Section 3.2, resulting in a total of 398 cross sections. To enhance simulation accuracy, these cross sections were interpolated at intervals of 10 to 20 m, producing a refined dataset with 3,064 cross sections for the hydraulic simulation.

Each cross section was assigned calibrated friction coefficients (K_s) with details provided in Appendix A.10. For flow input, the model accounted for discharges from 26 tributaries, as

well as the Pradella derivation and Martina restitution associated with EKW operations. The Pradella dam was included as an internal boundary condition.

Since the BAFU cross-sectional data spans from 2009 to 2016, the simulation period was set from 2008 to 2017 to provide representative 10-year simulation results. Model discharge inputs were provided by the corrected PREVAH-simulated discharge. In contrast to the BAFU measurements, which are point-based, the PREVAH model yields catchment-wide runoff predictions, enabling the extraction of simulated hydrographs for 26 tributaries as well as the Inn River's upstream hydrograph. Given the daily resolution of the PREVAH-simulated discharge data, the model was run to steady state for each day, and the corresponding hydraulic variables were saved for subsequent analysis. The 10-year time series includes a diverse range of hydrological events, allowing for the assessment of average hydraulic trends and persistent driving forcings over the study reach.

4.2.3 Post-processing of 1D Model Results for Riverbed Sediment Dynamics

After the 10-year simulation period, hydraulic variables from the original set of 398 cross sections (prior to interpolation) were extracted for analysis. The model outputs included discharge (Q), water surface elevation (WSE), wetted area (Ω), flow velocity (U), Froude number (Fr), energy grade line, mean flow depth (h), and mean bed elevation (b) at each cross section. The formulas used for calculating the Froude number and mean flow depth are provided in Appendix A.11.

In the BASEMENT model, the calculation of wetted area was simplified to improve computational efficiency. This simplification involved linear interpolation of the water surface elevation across sloped riverbanks, which could introduce a maximum absolute error of up to 0.08 m^2 in wetted area estimation at individual cross sections. As most errors were close to zero and typically much smaller than this maximum, their effect on subsequent analyses was considered negligible. Additionally, the cross section at the Pradella derivation was excluded from the analysis. Because the BASEMENT 4v model failed to accurately represent hydraulic variables at the site of water extraction.

To capture both spatial and temporal variability in the flow regime, a longitudinal profile of the Froude number was plotted, showing the median value along with the 1st–99th percentile range at each cross section, highlighting both typical and extreme flow conditions over the simulation period. Boundaries of the 12 segmented river reaches, their slopes, and potential driving forcings were annotated on the plot to provide context for interpreting spatial patterns.

The calculation of riverbed sediment dynamics was based on the assumption that the 1D modeling results are accurate and representative of actual river conditions. For detailed analysis, model outputs at the cross-sectional scale were further downscaled to vertical strips within each cross section, allowing for a more refined assessment of spatial variability in sediment processes.

Estimation of Bedload Transport for each Cross Section

For bedload transport estimation, cross sections were split into vertical strips with an average horizontal interval of 0.35 m, and hydraulic properties were analyzed within each vertical strip. The horizontal interval of 0.35 m was determined through the average measurement points from the cross sections extracted from DEM, which were denser than the BAFU-measured cross

sections. Therefore, an interpolation of measurement points was applied to the cross sections from BAFU to obtain denser vertical strips for calculation.

After subdividing the cross sections into i strips, their local velocities were estimated through the Gauckler-Strickler equation under the assumption of normal flow:

$$U_{i,\mathrm{NF}} = K_s R_{h,i}^{2/3} i_E^{1/2} \tag{4.4}$$

where $U_{i,\mathrm{NF}}$ is the normal flow velocity in strip i (m/s), K_s is the Strickler roughness coefficient ($\mathrm{m}^{1/3}/\mathrm{s}$), $R_{h,i}$ is the hydraulic radius of the strip i (m), and i_E is the energy slope. K_s and i_E were assumed to be the same for all strips in one cross section. K_s values were obtained thorugh calibration as Appendix A.10, while the i_E values were derived from the results of the model.

However, the normal flow assumptions may not ture and therefore required correction using a coefficient γ. The adjusted velocity U_i in strip i is then calculated as:

$$U_i = \gamma U_{i,\mathrm{NF}} \tag{4.5}$$

The value of the correction factor γ was determined by the relationship of mass conservation as Equation (4.6) and momentum balancing as Equation (4.7) as follows:

1. Mass conservation

$$Q = \sum_{i=1}^{N} \gamma U_{i,\mathrm{NF}}\, \Omega_i \tag{4.6}$$

   where Q is the total discharge (m^3/s) and Ω_i is the flow area of strip i (m^2).

2. Momentum balancing

$$\alpha = \frac{\sum_{i=1}^{N} \gamma U_{i,\mathrm{NF}}^3\, \Omega_i}{U^2 Q} \tag{4.7}$$

   where α is the kinetic energy correction factor, and U is the cross-section averaged velocity (m/s).

Mass conservation ensures that the total discharge is preserved by summing contributions from all strips. In the 1D hydraulic modeling performed in BASEMENT 4v, the model assumes uniform velocity across each cross section and does not resolve variations in the lateral or vertical velocity profile. Therefore, the kinetic energy correction factor α was set to 1 in the calculations. To obtain optimized γ, the residuals of the criteria of mass conservation and momentum balancing were minimized. The detailed procedure for γ determination is provided in Appendix A.12.

Based on the velocity correction, the bed shear stress τ_i for each strip was calculated as

$$\tau_i = \rho g \frac{U_i^2}{K_s^2 R_h^{1/3}}, \tag{4.8}$$

Most of the bedload formulas require the computation of the Shields parameter Θ_i for each strip, which characterizes the initiation of sediment motion:

$$\Theta_i = \frac{u_{*,i}^2}{g\,\Delta\,d_s}, \tag{4.9}$$

where $\Delta = \frac{\rho_s - \rho}{\rho}$ is the relative submerged density of the sediment (typically 1.65); d_s is the representative grain diameter (in meters), which is usually taken as d_{50}, but d_{84} is used in some cases (e.g., Recking (2013)); and $u_{*,i} = \sqrt{\tau_i/\rho}$ is the local shear velocity (in m/s).

For the bedload transport calculations, the grain size distribution (GSD) described in Section 3.4 was assigned to each river cross section according to the river segmentation defined in Table 5.1.

River sections exhibiting homogeneous characteristics were allocated the same GSD. Specifically, sections 1-4 were assigned the combined GSD from the Cinuos-chel sampling location; sections 5-7 were assigned the GSD from Zernez; sections 8-9 received the GSD from Ardez; and sections 10-12 were assigned the GSD from Ramosch. The transition between sections 4 and 5 corresponds to the location of the Zernez gravel mining site, which could influence the downstream GSD. Sections 8 and 9, characterized by relatively high flow intensity compared to adjacent reaches, likely have similar sediment transport capacities. Finally, sections 10–12 are located downstream of the Pradella dam, which acts as a barrier to upstream sediment transport and thus alters the downstream GSD.

Eight bedload transport formulas, summarized in Table 4.2, were applied to each strip. Six of these consider uniform GSD, while two incorporate the effects of mixing GSD and hiding effect. The dimensionless bedload transport rates (W^*, Φ) predicted by these formulas were converted to dimensional values, and individual strip contributions Q_{bi} were summed to obtain the total bedload transport rate Q_b for each cross section. The detailed formulations are provided in Appendix A.13.

Table 4.2: Main characteristics of the bedload transport formulas used

Type	Formula Name	Experimental Conditions & Validity Domain
Uniform GSD	Meyer-Peter and Müller (1948)	Flume data; gravel-bed streams with
	Parker (1979)	Flume and field data; gravel-bed rivers
	Parker-Klingeman-McLean (1982)	Field data; gravel-bed rivers
	Rickenmann (1991)	Flume data
	Wong & Parker (2006)	Reanalysis of Meyer-Peter & Müller using their own flume data
	Recking (2013)	Flume and field data; sand- and gravel-bed rivers
Mixed GSD	Parker (1990)	Field data; only gravel movement considered
	Wilcock & Crowe (2003)	Field data; mixed sand/gravel sediment

To compare sediment transport efficiency across different formulas, the ratio of bedload transport to water discharge (Q_b/Q) was calculated daily at each cross section over the 10-year simulation period. For each cross section, the probability density function (PDF) of Q_b/Q for each formula was derived from these daily values. The expected value, representing sediment transport efficiency, was computed as

$$E\left[\frac{Q_b}{Q}\right] = \int \left(\frac{Q_b}{Q}\right) \cdot \mathrm{pdf}\left(\frac{Q_b}{Q}\right) d\left(\frac{Q_b}{Q}\right) \tag{4.10}$$

this metric allowed direct quantitative comparison of the predicted sediment transport efficiencies and uncertainties associated with each bedload transport formula.

Discharge Resolution Effects on Shear Stress and Sediment Transport

The model used daily discharge data from corrected PREVAH simulations, which did not capture short-term flow variability and potentially underestimated high-flow events that drive sediment transport. Since bedload transport is primarily governed by shear stress (τ), its sensitivity to temporal resolution was assessed at three cross sections near BAFU gauging stations (Cinuos-chel, Tarasp, and Martina).

For each of these cross sections, shear stress (τ) at hourly resolution was calculated using the hourly BAFU-measured discharge and water surface elevation, together with the measured cross-sectional geometry through Equation (4.8). These values were then compared to shear stress estimates derived from the daily model simulation using the same Equation (4.8). The distributions of shear stress values from both the daily simulation results and hourly observations were plotted as boxplots side by side to evaluate the impact of discharge temporal resolution on sediment transport estimation.

Estimation of Erosion and Aggradation Between Cross Sections

The temporal change in bed elevation due to the divergence of bedload transport between two consecutive cross sections can be described by the sediment continuity equation, as shown in Equation (4.11):

$$\frac{d\eta}{dt}W_b = -\frac{dQ_b}{dx} \tag{4.11}$$

where η and W_b are the bed elevation (m) and channel bottom width (m) between two consecutive cross sections, Q_b is the bedload transport rate at the cross sections (m^3/s), and x is the longitudinal distance between two consective cross sections (m).

The left-hand side of Equation (4.11) characterizes the rate of bed elevation change over time, integrated across the channel bottom width. The right-hand side indicates the spatial gradient of the bedload transport rate between adjacent cross sections from upstream to downstream: a decrease Q_b in the downstream direction indicates sediment deposition and riverbed aggradation, whereas an increase indicates bed erosion.

For each day of the 10-year simulation period (2008–2017), $-dQ_b/dx$ values were computed using bedload transport rates from the formulas listed in Table 4.2. This involved calculating the change in Q_b between consecutive cross sections from upstream to downstream and dividing by the distance between them, yielding erosion or deposition rates. Probability density functions (PDFs) of these rates were generated for each cross section using results from all formulas, and the expected value of each PDF was used to characterize typical erosion or aggradation intensity.

The left-hand side of Equation (4.11), representing observed bed elevation changesh, was estimated using BAFU-measured cross sections from the periods 2000s–2010s and 2010s–2020s. For each pair of consecutive cross sections, the product of the average bed elevation change and mean channel bottom width provided an empirical rate of riverbed change. These observational results were then compared with the model-based results to evaluate the consistency in trends of erosion and aggradation. Comparing model results with changes from 2000s–2010s assesses whether past trends have persisted or shifted, with consistency suggesting stable conditions and divergence indicating possible new external influences. Comparison with 2010–2020 measurements serves to validate the model and highlight any factors not captured within the modeling framework.

5 Results

5.1 River Characterization and Segmentation

Based on catchment-scale criteria, the study river was divided into 12 sections, as illustrated in Figure 5.1, with each section exhibiting relatively homogeneous characteristics. Detailed summaries of each section are provided in Tables 5.1.

Section 1 is characterized by a meandering channel flowing through erosive sedimentary rock. Downstream, the river enters a region of resistant bedrock and becomes valley-confined. Section 2 is notable for its steep riverbed, with a slope of 2.8% while the slope of section 3 decreases to 1.2%. Section 4 is moderately confined and features a straight channel. Sections 5 and 7, located near the villages of Zernez, Susch, and Lavin, are classified as human-confined due to anthropogenic interventions of banks. Section 6, situated between these villages, is straight and with no obvious sediment sources or sinks. Section 8 is valley-confined and distinguished by a relatively high slope of 1.5% compared to adjacent sections. Section 10 encompasses the Pradella dam. Section 11 is an extended erosive reach with several segments exhibiting multiple channels. Finally, section 12, as it approaches Martina, is human-confined and flows through resistant bedrock.

This segmentation provides a framework for analyzing the spatial variability of river morphology and processes along the study reach.

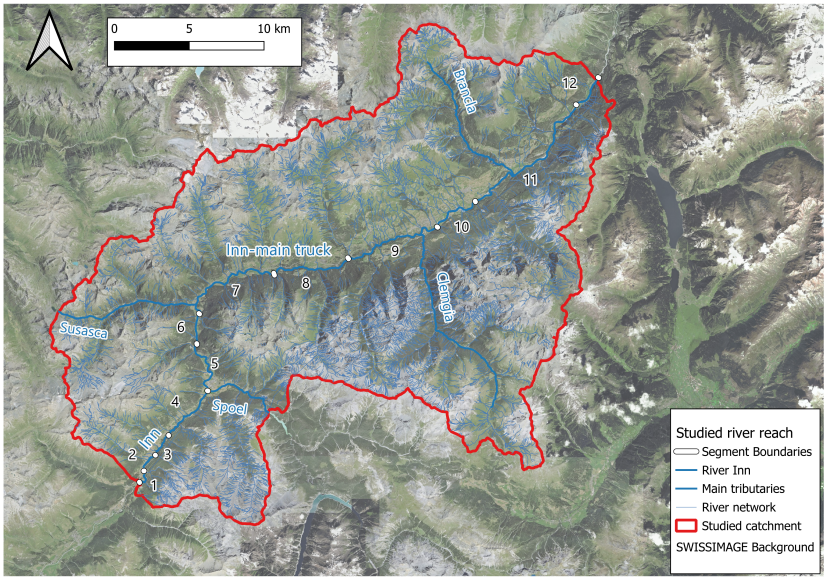

Figure 5.1: Segmentation of the Inn River into 12 sections

Table 5.1: Overview of river channel segments classified by lithology, slope, confinement type, morphology (sinuosity, planimetric and altimetric features), sediment sources from debris flow (DF.) and tributaries (Trib.), and identified sediment sinks.

Index	Distance range (km)	Lithology	Slope (%)	Confinement	Morphology			Sed. sources		Sed. sinks
					Sinuosity	Planimetric	Altimetric	DF.	Trib.	
1	0 - 1.335	Sedimentary rock	1.241	Moderately conf.	1.54	Meandering	Point and alternate bars	1	\	\
2	1.335 - 2.901	Metamorphic rock	2.826	Valley conf.	1.11	Sinuous	Plane bed	1	1	\
3	2.901 - 4.796	Metamorphic rock	1.200	Valley conf.	1.1	Straight	Plane bed	2	1	\
4	4.796 - 9.495	Metamorphic & sedimentary rock	0.935	Moderately conf.	1.1	Straight	Mostly plane bed	2	1	\
5	9.495 - 14.302	Sedimentary rock	0.730	Human conf.	1.38	Sinuous	Point and alternate bars	\	3	One gravel mining
6	14.302 - 16.598	Sedimentary rock	0.507	Moderately conf.	1	Straight	Plane bed	\	\	\
7	16.598 - 25.205	Metamorphic & sedimentary rock	0.968	Moderately with partial human conf.	1.45	Sinuous	Mostly plane bed	\	4	\
8	25.205 - 31.406	Metamorphic & sedimentary rock	1.595	Valley conf.	1.11	Sinuous	Plane bed	\	1	\
9	31.406 - 39.440	Metamorphic rock	0.950	Moderately with partial human conf.	1.18	Sinuous	Plane bed	2	5	\
10	39.440 - 43.466	Sedimentary rock	0.650	Moderately with partial human conf.	1.21	Sinuous (84%) & Braiding (16%)	Point and alternate bars	2	2	Pradella dam
11	43.466 - 55.328	Sedimentary rock	0.661	Moderately with partial human conf.	1.18	Sinuous (27%) & Anabranching (11%) & Wandering (62%)	Point and alternate bars	9	1	One gravel mining
12	55.328 - 58.051	Metamorphic rock	0.488	Human conf.	1.07	Straight	Point and alternate bars	\	1	\

5.2 Evolutionary Trajectories—Global View

Figure 5.2 compares the active river width in 1946 and 2021, presenting both the mean width and its variability band for each river section. The results indicate that, from upstream to downstream, sections alternated between periods of widening and narrowing. Section 10 exhibited a pronounced change in width, which is the section of the Pradella dam.

Figure 5.2 depicts only the initial and final conditions of the surveyed period. The full temporal series in Figure 5.3 shows that active river width fluctuated repeatedly between widening and narrowing phases between 1946 and 2021. It further delineates periods of channel widening, narrowing, and stability by comparing normalized width changes to the uncertainty from width extraction. The river experienced sustained narrowing during 1960–1972 and 1990–1996, while phases of channel widening occurred between 2008–2014 and 2018–2021.

Figure 5.4 illustrates the trajectories of centerline migration along the river from 1946 to 2021, highlighting active, inactive, and stable periods based on comparisons with the standard deviation bands. The analysis focused on active periods of centerline migration in 1958–1960 and 2005–2011, which were characterized by fragmented activity across sections. Specifically, the 1958–1960 active period was most pronounced in sections 3–8, while the 2005–2011 period primarily affected sections 1–3 and 8–11.

Figure 5.5 provides a sectional summary of other morphodynamic features, including vegetation bars, alternate bars, braided reaches, and river flow paths. These morphodynamic processes were mainly concentrated in sections 5, 10, and 11, reflecting sectional morphodynamic activity rather than whole-river behavior.

Based on the overall trends in centerline migration and active width changes, potential external forcings were identified and summarized in Figure 5.6, which provides a comprehensive overview of influencing factors across the entire catchment.

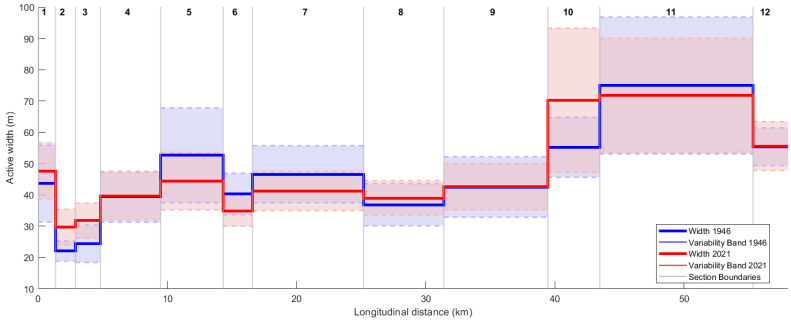

Figure 5.2: Weighted mean active width and variability (half of the 16th–84th percentile) for 12 river sections in 1946 and 2021

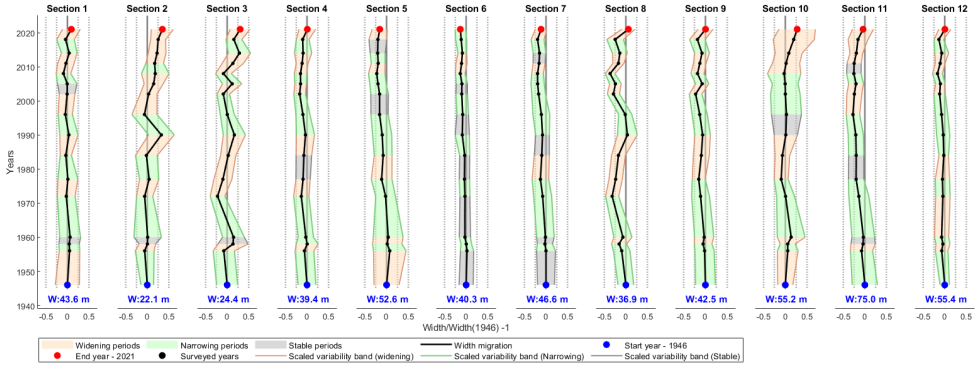

Figure 5.3: Evolutionary trajectories of normalized active width and scaled variability (1946–2021) across 16 survey years (W_{blue}: active width in 1946). Periods of widening or narrowing are identified when changes exceed uncertainty thresholds; changes within uncertainty are considered stable (entire river: narrowing in 1960–1972 and 1990–1996; widening in 2008–2014 and 2018–2021).

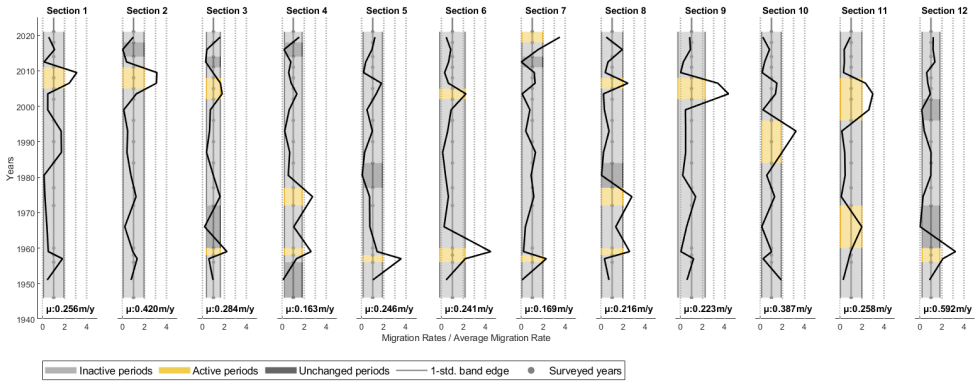

Figure 5.4: Evolutionary trajectories of normalized migration rates with standard deviation (*std.*) bands (1946–2021) across 16 survey years (μ: average centerline migration rate). Periods are classified as active, inactive, or stable based on comparisons with the *std.* bands per river section (active periods: 1958–1960 for sections 3–8; 2005–2011 for sections 1–3 and 8–11).

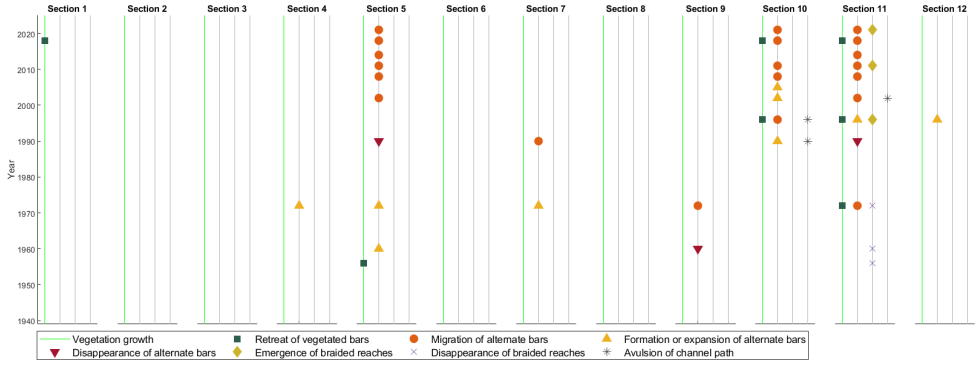

Figure 5.5: Evolutionary trajectories of other morphological processes (1946–2021) across 16 survey years (intensive changes observed in sections 5, 10, and 11)

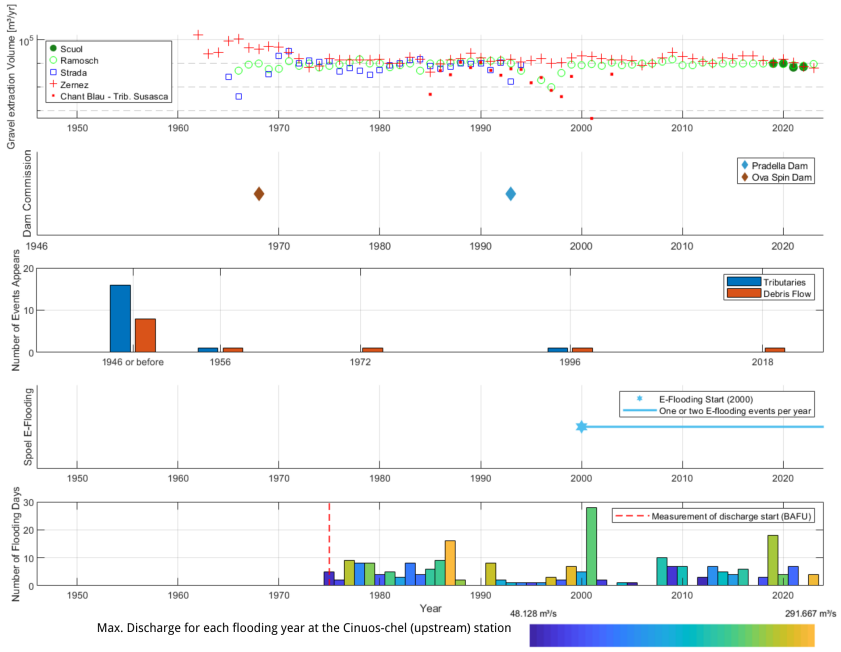

Figure 5.6: Summary of external forcings in the study catchment—global overview supporting the identification of potential drivers of active width (narrowing: 1960–1972, 1990–1996; widening: 2008–2014, 2018–2021) and centerline migration (active periods: 1958–1960, 2005–2011)

5.3 Evolutionary Trajectories—Sectional View

River morphodynamics and their driving forces were analyzed at the sectional scale to enable a detailed understanding of river shape changes in response to various external forces. For each river section, changes in active width, centerline migration, and other morphological processes were systematically compared with corresponding sectional external drivers. The analysis focuses on river sections with significant or representative morphological changes, as illustrated in Figure 5.7 to Figure 5.9.

Sections 7 and 8 in Figure 5.7 were selected to illustrate possible relationships between flooding events and active channel width, using examples of both relatively low and high flood intensity to enhance the comparative analysis. Sections 5 and 11 in Figure 5.8 were emphasized due to their pronounced other morphological changes, including changes in alternate bars, braiding reaches, and flow path, allowing identification of key external forcings behind these responses. Section 10 in Figure 5.9 is highlighted as the only section directly influenced by the Pradella dam and has intensive changes in alternate bars and flow path.

For all other sections, detailed summaries of morphological changes and their associated external drivers are provided in Appendix A.8. This sectional approach enables an understanding of how specific local external factors drive spatially heterogeneous river morphodynamics.

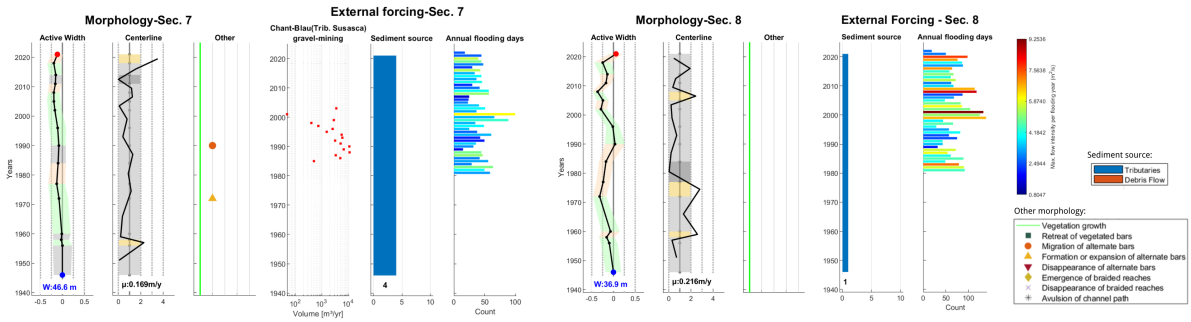

Figure 5.7: Comparison of external flooding forcing and active width changes in Section 7 and 8 (W_{blue}: active width in 1946, μ: average centerline migration rate)

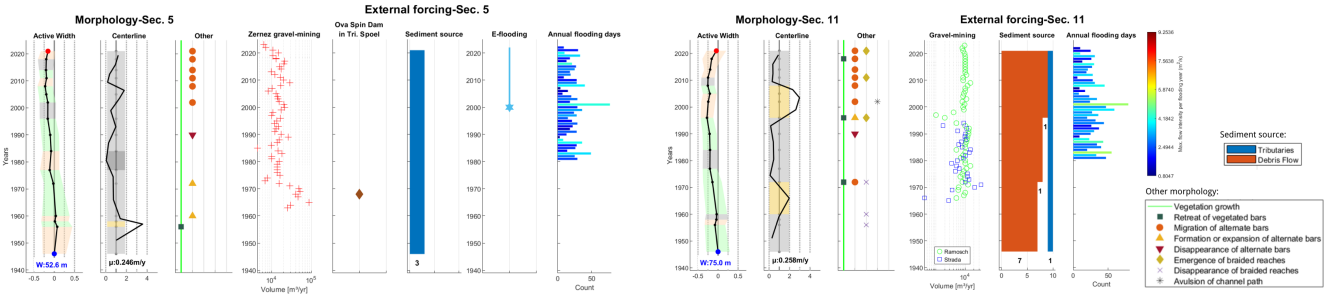

Figure 5.8: Analysis of intense morphological processes including alternate bars, braiding, and flow path changes in Section 5 and 11 (W_{blue}: active width in 1946, μ: average centerline migration rate)

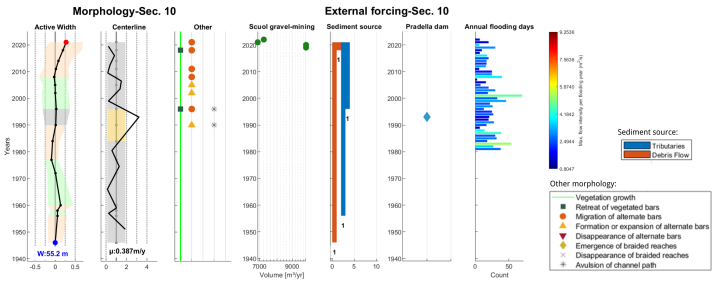

Figure 5.9: Influence of Pradella Dam and associated morphological changes in Section 10 (W_{blue}: active width in 1946, μ: average centerline migration rate)

5.4 Further Analysis of River Active Width

The active width values were further analyzed to investigate their variability, spatial patterns, and relationships with other channel properties (Figures 5.10, 5.11, and 5.13).

Figure 5.2 reveals a general trend where sections with larger mean active widths also exhibit greater variability. This relationship was further investigated in Figure 5.10, which shows scatter plots of mean active width versus variability for each section and survey year. Excluding Sections 10 and 11, the data display a strong linear relationship, with variability averaging approximately 20% of the weighted mean active width for each section. However, this relationship does not

hold for Sections 10 and 11, where the data points are more scattered with exceptionally large width values.

The relationship between active width variability and the spatial correlation scale (Taylor scale) is assessed using autocorrelation analysis (Figure 5.11). On a log-log scale, river sections with higher active width variability are associated with longer Taylor microscales, indicating that larger width variations tend to persist over greater spatial distances before being disrupted by smaller-scale fluctuations.

To validate the extracted active width data, a longitudinal comparison with BAFU-measured bottom width in the 2010s is presented in Figure 5.12. Both the active width and bottom width exhibit similar spatial variability along the river. The bottom width is generally slightly narrower than the active width. Additional comparisons for the 2000s and 2020s are provided in Appendix A.9.

Figure 5.13 overlays the section-averaged, normalized bottom width onto the evolutionary trajectories of normalized active width (from Figure 5.3), allowing direct comparison of temporal trends and potential relationships between the two width metrics.

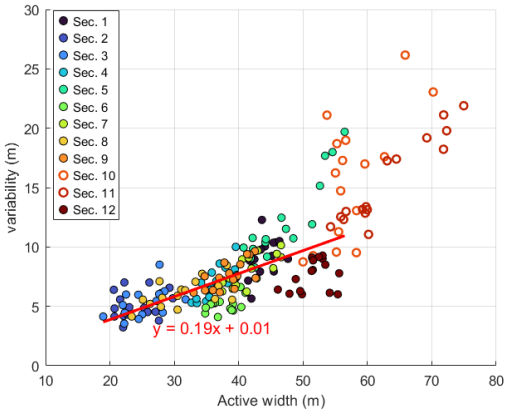

Figure 5.10: Weighted mean of active width vs. variability for each river section, with linear fit excluding sections 10 and 11

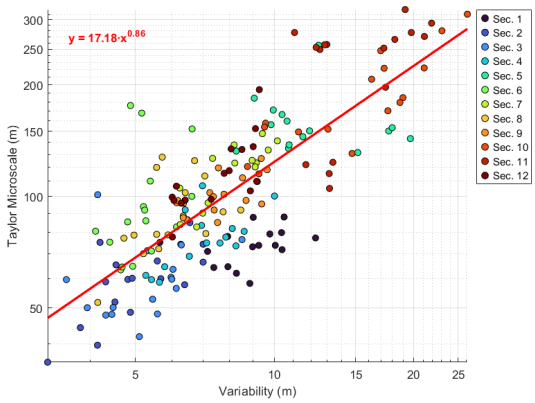

Figure 5.11: Log-log relationship between active width variability and spatial correlation scale (Taylor microscale) for each section

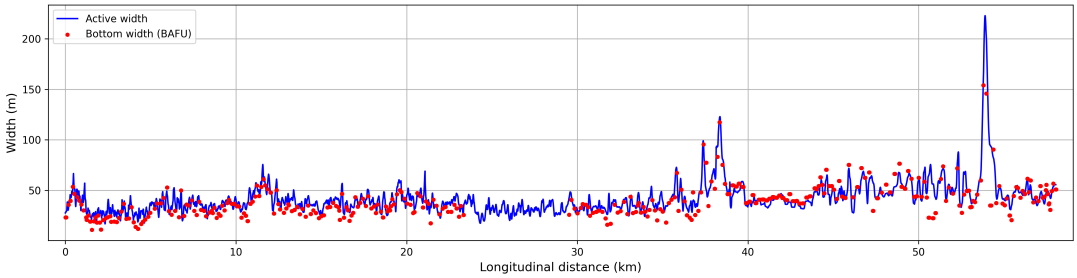

Figure 5.12: Longitudinal comparison of active Channel width and BAFU-measured bottom width along the Inn River in the 2010s

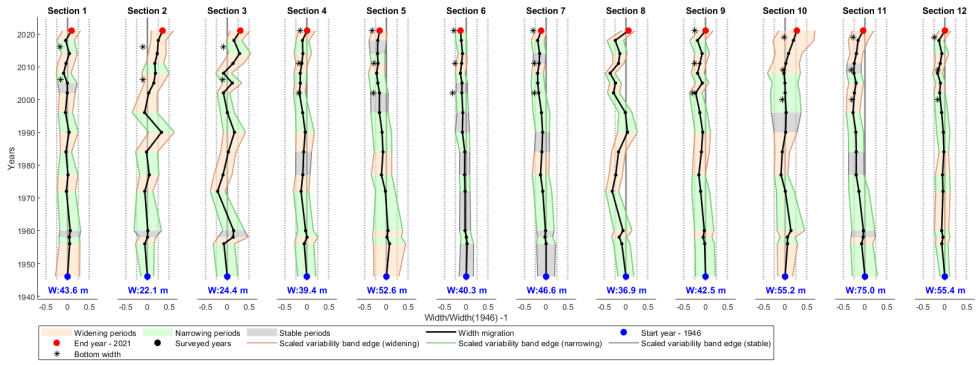

Figure 5.13: Evolutionary trajectories of normalized active width and scaled variability (1946–2021), alongside normalized BAFU-measured bottom width, across 16 survey years (W_{blue}: active width in 1946), highlighting widening, narrowing, and stable periods for each river section

5.5 Sediment Dynamics

5.5.1 Flow Regime Characterization via Froude Number—1D Modeling

The spatial and temporal variability in flow regime across the study reach is illustrated in Figure 5.14, which shows the longitudinal profile of median Froude numbers over the 10-year simulation period (2008–2017). The 1–99% inter-percentile range at each cross section highlights both typical and extreme flow conditions. Clear spatial patterns emerge, with distinct variations in Froude number distribution along the reach. The figure also displays the boundaries of the 12 segmented river sections and their corresponding slopes, together with potential driving forcings, offering insight into the factors influencing local flow dynamics.

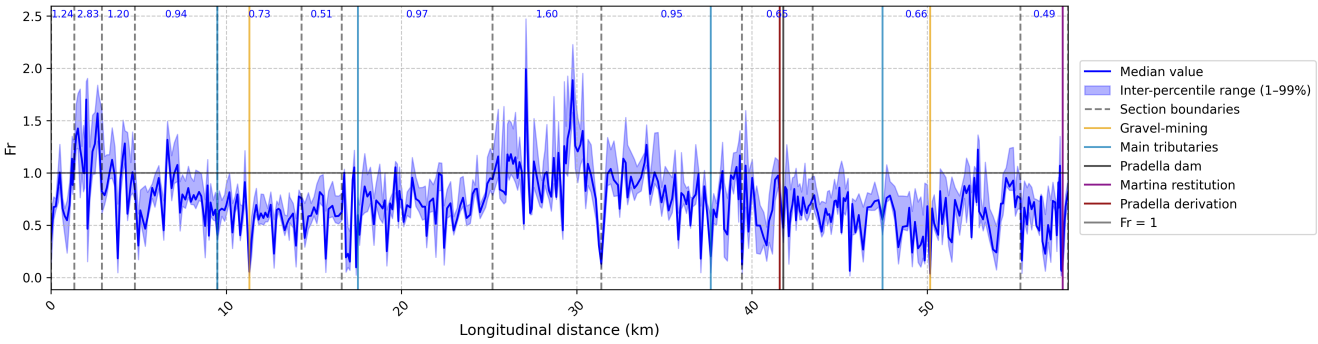

Figure 5.14: Froude number profile along the Inn River: median and 1–99% range with external forcings; 12 segmented reaches with bed slope labeled between section boundaries

5.5.2 Bedload Transport and Shear Stress—1D Modeling

Figure 5.15 presents the ratio of bedload transport to water discharge (Q_b/Q) along the Inn River, computed using several bedload transport formulas. The ratio results, derived from 10-year PDFs at each cross section, are plotted to illustrate differences in transport efficiency and variability between formulas.

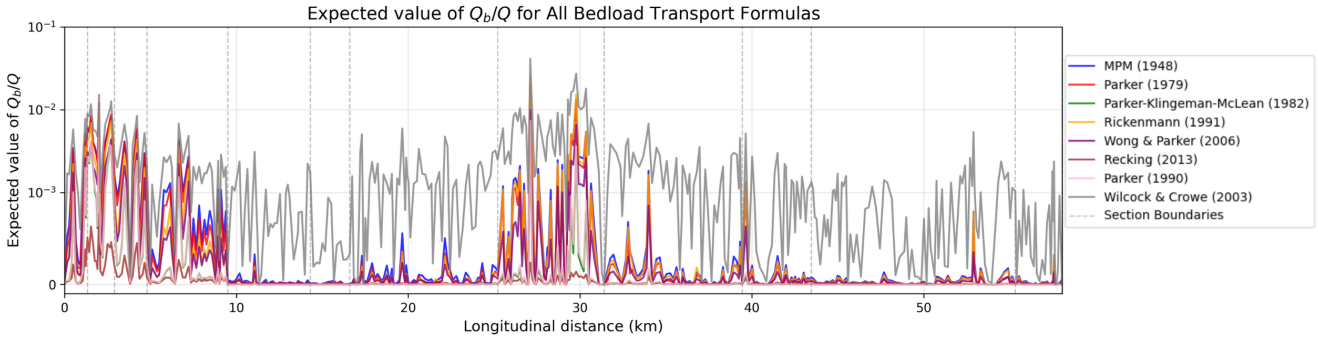

Figure 5.15: Expected values of the Q_b/Q ratio derived from probability density functions over a 10-year simulation period for each bedload transport formula along the Inn River

Figure 5.16 illustrates the effect of discharge temporal resolution on shear stress estimation and further bedload sediment transport. At the Cinuos-chel, Tarasp, and Martina cross sections, where the BAFU-measured hourly discharge is available, shear stress (τ) distributions based on hourly measured data (grey) are compared to those derived from daily simulated discharge (blue).

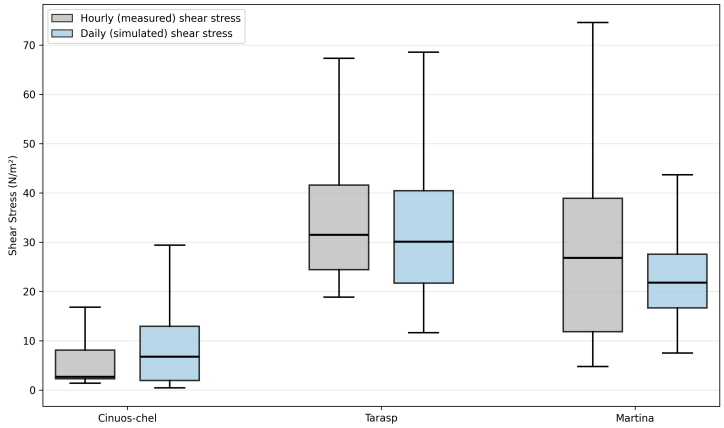

Figure 5.16: Comparison of bed shear stress (τ) distributions at Cinuos-chel, Tarasp, and Martina: hourly shear stress from measured discharge (grey) versus daily shear stress from simulated discharge (blue)

5.5.3 Riverbed Changes: Model vs. BAFU Measurements

Figure 5.17 compares estimated rates of riverbed erosion and aggradation derived from estimated bedload tranpsort of 1D modeling (rectangular markers) with BAFU-measured riverbed change rates for the periods 2000s–2010s and 2010s–2020s (dots). Gaps exist for river sections without BAFU measurements. Vertical lines mark locations of major potential driving forces for aggradation or erosion along the study reach.

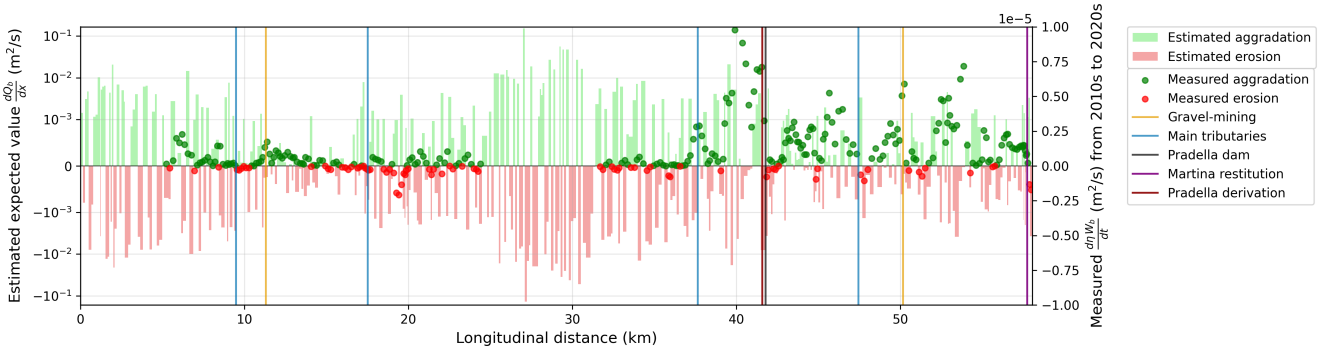

(a) BAFU-measured bed elevation changes integrated across the channel bottom width (2010s–2020s), compared with model-predicted erosion and aggradation rates using 2010s topography and simulated discharge from 2008 to 2017.

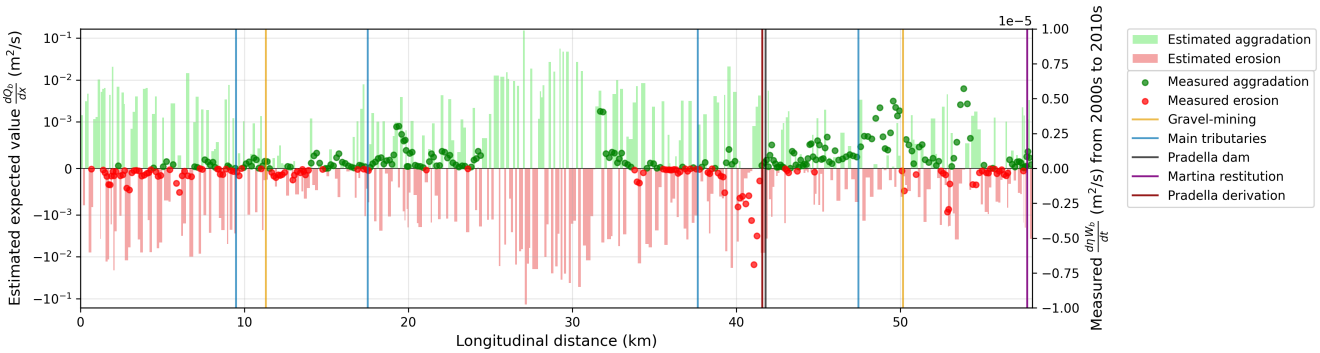

(b) BAFU-measured bed elevation changes integrated across the channel bottom width (2000s–2010s), compared with model-predicted erosion and aggradation rates using 2010s topography and simulated discharge from 2008 to 2017.

Figure 5.17: Comparison of modeled erosion and aggradation rates with BAFU-measured riverbed elevation changes integrated across the channel bottom width along the Inn River, highlighting cross sections with potential external forcings.

6 Discussion

6.1 River characterization and segmentation

The river characterization and segmentation conducted in this study identified 12 distinct sections, each exhibiting unique characteristics. It is assumed that within each section, morphological changes follow similar trends and are caused by similar external drivers due to the relative homogeneity of their features. This segmentation forms the basis for evolutionary trajectory analysis and helps identify the external drivers influencing the historical morphological evolution of the river.

However, this classification is based on current river conditions. Historical river characteristics may have differed significantly, particularly due to anthropogenic interventions such as the construction of levees or embankments, which could have altered the degree of river confinement over time. For example, sections 5, 7, and 12 may have been only moderately confined in the past, potentially affecting both the segmentation and the observed patterns of morphological activity in these reaches. Therefore, future studies should incorporate historical river characteristics from the study period to ensure that any significant changes affecting segmentation are properly accounted for.

6.2 Evolutionary Trajectories—Global view

6.2.1 Influence of Temporal Resolution on Active Width Analysis

Figure 5.2 compares the active river width in 1946 and 2021, highlighting alternating patterns of narrowing and widening across river sections. However, the comparison limited to these two time points fails to fully capture the full evolutionary trajectory of the active width over the 75-year period. As shown in Figure 5.3, most sections exhibit temporal alternations between narrowing and widening, suggesting that short-term dynamics may be obscured when only the start and end points are considered. For example, while Section 10 in Figure 5.2 shows significant widening from 1946 to 2021, a finer temporal resolution reveals two distinct widening phases during the interval. Similarly, sections 12 and 9 show little net change in active width when comparing 1946 and 2021, but they experienced multiple cycles of narrowing and widening during the time period. These observations illustrate that limited survey frequency may smooth out transient dynamics, leading to an oversimplified interpretation of river behavior.

This limitation highlights the need for increased temporal sampling in future river monitoring, as high-frequency data are crucial for capturing the dynamics of channel evolution and informing adaptive management strategies.

6.2.2 Identification of Morphological Driving Forces for Global River Trend

The evolutionary trajectories of active width, centerline migration, and other morphological processes are illustrated in Figures 5.3 to 5.5. Both active width and centerline migration display periods of morphological trend across multiple river sections. The active width generally narrows

during 1960–1972 and 1990–1996, while periods of widening are observed in 2008–2014 and 2018–2021. Centerline migration is active from 1958–1960 in sections 3–8, and from 2005–2011 in sections 1–3 and 8–11. In contrast, the trajectories of bar, braiding, and avulsion activities (Figure 5.5) do not display clear global trends, and will therefore be only analyzed at the sectional scale. This suggests that such processes are likely governed by local factors, and their influences may not propagate far downstream due to varying geomorphic, hydrologic, and anthropogenic characteristics between sections. Accordingly, the external drivers affecting bar dynamics, braiding, and avulsion may differ from those controlling active width and centerline migration. Therefore, effective river management should account for both local and reach-scale contexts, with the appropriate focus depending on the specific morphological processes of focus.

To identify potential drivers, the timing of major changes in active width and centerline migration was compared with external factors in Figure 5.6. The results indicate a strong correlation with flood events, as highlighted by the temporal overlap shown in Figure 6.1

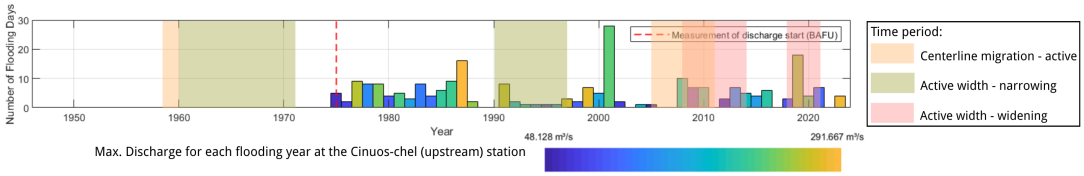

Figure 6.1: Temporal overlap between flooding events and periods of active width and centerline migration change

Analysis of Global Trend in Active Width

Figure 6.1 shows that periods of active width narrowing generally coincide with prolonged intervals of low flood intensity and duration, while widening is typically associated with the sudden occurrence of high-flooding events following low-flooding periods. Specifically, the narrowing observed from 1990 to 1996 corresponds to years with prolonged low flooding, whereas the widening periods of 2008–2014 and 2018–2021 were sudden high-flooding years following low-flooding intervals.

The possible explaination could be the influence of the flow regime on the vegetation establishment and sediment deposition. During low-flooding periods, riverbanks are more stable, allowing vegetation to grow and further stabilize these banks, which leads to channel narrowing and reduced lateral migration. Over time, the accumulation of finer sediments due to the low sediment transport capacity during this period can reinforce this narrowing trend. In contrast, when high floods occurs after low-flood periods, these newly vegetated and sediment-accumulated banks become highly susceptible to erosion. High flows rapidly mobilize accumulated sediment and remove vegetation, resulting in channel widening and increased morphological activity. This cyclical interaction emphasizes the role of hydrological variability in shaping river morphology.

In the global view of river morphological changes, these findings imply that the contrast of prolonged low floods with subsequent intense high floods is critical for generating observable morphological changes throughout the entire river reach. However, as discussed in Section 6.2.1, the interpretation of these trends is subject to the limitations of temporal resolution in mor-

phological surveys. For instance, a possible widening event due to high floods in 1991 is not reflected in the constructed trajectories due to the lack of imagery between 1990 and 1996.

The interval from 2002 to 2008, characterized by prolonged low flooding without a clear trend of channel narrowing, further highlights the complexity of these dynamics. This period directly followed the extreme floods of 2001, which was the year with the longest flood duration and relatively high intensity within the study period. It is possible that the 2001 flood uprooted vegetation and flushed significant volumes of sediment downstream, inhibiting immediate vegetation regrowth and delaying sediment accumulation. As shown in Figure 5.3, some channel sections did exhibit the expected narrowing, while others initially widened before narrowing, indicating spatial variability in recovery rates and responses to disturbance, likely related to localized channel and floodplain characteristics.

These findings provide a baseline for predicting future changes in river active width. The observed cycles of high and low flooding are unlikely to produce fundamental or permanent alterations to river width and riparian areas. The short-term widening due to high floods is expected to be followed by narrowing during subsequent low-flow periods. However, special attention should be given to extreme flood events that occur with both high frequency and intensity within a year, as these may trigger irreversible morphological changes in the river system.

Analysis of Global Trend in Centerline Migration

The periods of active centerline migration often coincide with phases of active width narrowing or widening, as illustrated in Figure 6.1. As described in Section 4.1.2, the centerline is extracted by connecting the centroid points of the active channel width. Consequently, changes in centerline position and active width are inherently linked through processes of riverbank erosion and deposition. Similar to active width dynamics, centerline migration is influenced by low- and high-flooding events. However, Figure 6.1 also reveals intervals where significant changes in active width occurred without corresponding active centerline migration. This can be attributed to situations where erosion and deposition are balanced between both banks, resulting in channel widening or narrowing without a notable shift in the channel centerline.

Centerline migration thus provides complementary yet distinct insights into river morphodynamics, as it is particularly sensitive to asymmetries in bank erosion and sedimentation activity. Factors such as hydrological variability, differences in bank material properties, and the planform curvature of each bank can contribute to patterns of centerline movement. To further understand these dynamics, future studies should employ process-based riverbank erosion models capable of integrating these variables, thereby enabling more accurate prediction and understanding of centerline behavior.

Centerline migration trends also exhibit fragmentation along the river reach. One likely factor is local channel confinement, such as levees or embankments, which can disrupt the continuity of centerline adjustment and limit the river's capacity for lateral migration. For example, the otherwise active centerline migration observed between 2005 and 2011 is interrupted in sections 4 to 7, likely due to human-induced bank confinement.

6.2.3 Identification of Morphological Driving Forces for Sectional River Trend

A global analysis of river morphological trends identifies drivers affecting the whole reach, but may overlook important localized changes critical for comprehensive morphodynamic assessment and effective management. Examining morphological changes at the sectional level allows for the detection of responses to local drivers, which can be obsured in a global perspective.

Analysis of Active Width and Centerline Migration in Section 7 and 8

Figure 5.7 contrasts two adjacent river sections with their morphological evolution and local forces. Section 7 shows a consistent narrowing trend with only brief widening phases, while Section 8 displays alternating phases of narrowing and widening over the same period. This divergence can be attributed primarily to local flood regimes. Section 7 is characterized by persistently low flood intensity, corresponding with sustained channel narrowing. In contrast, Section 8 experiences pronounced variability in flood intensity. Its cycles of high and low flood events correspond closely to observed alternations between channel widening and narrowing. Widening occurs rapidly in response to high flood events, while narrowing happens gradually during periods of low flood intensity.

For the sectional analysis, unit discharge was calculated to characterize local flood regimes, facilitating a direct and meaningful comparison between sections. These findings validate the high-low flood effects identified in the global analysis (Section 6.2.2), and show that such effects are more pronounced at the sectional scale. A prolonged low-flood interval and a sudden high flood following a low-flood period are not necessary preconditions. Relative shifts between high and low flood periods are sufficient to drive local morphological changes in active width

Similarly, the centerline migration of section 8 is more active than that of section 7, due to the intrinsic connection between the centerline and the active width as discussed in Section 6.2.2. This suggests that river sections with higher variability in flooding tend to experience more active changes in active width and centerline.

Analysis of morphological processes in Section 5 and 11

Figure 5.8 presents the morphological evolution and local influencing factors for Sections 5 and 11. Both sections exhibit active alternate bar dynamics and are associated with long-term gravel-mining operations, highlighting a strong relationship between them. The disappearance of alternate bars in both sections around 1990 corresponds with a period of relatively high gravel extraction volumes. Conversely, the formation or expansion of alternate bars in Section 5 in 1972 and in Section 11 in 1996, both coincided with reductions in gravel extraction.

The interplay between sediment supply, gravel extraction, and sediment transport capacity is a key factor influencing alternate bar dynamics. In the case of the sediment supply, section 5 has three tributaries, while section 11 receives input from nine debris flows and one tributary. Assuming transport capacity is relatively stable, the balance between sediment supply and gravel extraction becomes important. Where sediment supply exceeds gravel extraction, sufficient material is available for bar development, and alternate bars are more likely to form or expand. Conversely, if gravel extraction surpasses supply, sediment deficits arise, leading to the

disappearance of alternate bars as there is insufficient material to maintain them. In sections without extensive gravel mining (see Appendix A.8), a relative equilibrium between sediment supply and transport capacity can be maintained as a balanced sediment budget, supporting a morphologically stable, often plain-bed channel with limited or no alternate bar development.

In Figure 5.8, the consistent migration of alternate bars coincides with the e-flooding events starting from in 2000 for both section 5 and 11. This suggests that e-floods successfully activate morphological processes within this river section, as they are specifically designed to mobilize sediments and reshape bars, thereby enhancing in-channel morphodynamics (Hashemi et al. (2023)). Section 5 is directly connected to the Spoel tributary (see Figure 2.1) and is therefore strongly influenced by both sediment and discharge inputs from these e-flooding events. The increased sediment transport together with increased sediment supply results in cycles of erosion and deposition, which in turn drive the downstream migration of alternate bars. This feedback highlights the effectiveness of targeted e-flooding in restoring dynamic river morphology.

It is difficult to determine the downstream influence range of e-flooding after the Spoel confluences with the Inn River. Although Section 11 exhibits consistent alternate bar migration, no distinct in-channel morphological changes are observed between Sections 5 and 11 (see Figure 5.5). While suspended sediment or flow signals from e-floods may be briefly detectable up to 30 km downstream in section 11, bar migration and channel morphology in these distant, dynamic reaches should be primarily controlled by local factors. According to Table 5.1, Section 11 is characterized by erosive rock types and the highest number of sediment sources among all studied sections, making it particularly responsive to local geomorphic drivers. Around 2000, several significant events occurred in this reach: a debris flow was activated in 1996, the Strada gravel-mining site stopped operation in 1994, and the gravel extracted at Ramosch site has become consistent since 2000. The combination of newly available sediment from the debris flow and the reduction in gravel extraction resulted in a substantial increase in sediment availability within the channel. This enhanced sediment supply facilitated not only the formation and expansion of alternate bars but also provided abundant material for flood flows to mobilize, leading to pronounced erosion and deposition cycles for alternate bar migration. When sediment input from debris flows exceeds the transport capacity of a single-thread channel, the excess material is deposited overbank, prompting the development of multiple flow threads and thus a transition to a braided channel pattern. The braiding, in turn, creates multiple flow paths that increase the likelihood of channel avulsion, which was observed in 2002 following the initial braiding in 1996.

Such interactions between sediment supply, bar migration, channel braiding, and avulsion in section 11 can sustain high morphological dynamism for years, continually reshaping both channel and floodplain. Similar processes have been observed in alpine rivers like the Rhone and Illgraben, where repeated debris-flow inputs drive increased fluvial erosion and transport for years, leading to intense geomorphic activities (Haas et al. (2004)).

To further support this explanation, it would be necessary to compare the annual sediment supply from tributaries and debris flows in each section with the corresponding volume of gravel extracted. Examining sediment budget components in a more quantitative way would offer clearer insights into how these dynamics influence bar morphology, channel braiding, and avulsion across different sections of the river.

Analysis of Influence of Dam Construction in Section 10

During the construction of the Pradella Dam (see Figure 5.9), an anthropogenic intervention resulted in a river avulsion event. To enable dam construction in 1993, the river channel was temporarily rerouted, with the flow returned to its original course after completion. This engineering work corresponded with two observed avulsion events in 1990 and 1996.

Such abrupt, human-induced changes in river course caused a disruption in sediment transport and deposition regimes, leading to channel instabilities. These instabilities activated the development and downstream migration of alternate bars, as the river adjusted to its modified state. This example highlights the impact of engineered interventions on river morphodynamics.

6.2.4 Further Analysis of River Active Width

Relationship Between Weighted Mean and Variability of River Active Width

Figure 5.10 illustrates the relationship between mean active width and its variability across river sections. The results indicate that wider channels tend to exhibit more pronounced spatial fluctuations in active width. This may be attributed to increased lateral space for channel migration, as well as the likelihood that broader active widths reflect more erodible banks and moderate confinement, both factors that enhance variability. In contrast, Sections 2, 3, and 8, characterized by relatively narrow active widths and low variability, are located within confined valley settings (see Table 5.1).

A threshold is visually identified at an active width of approximately 55 m in Figure 5.10. Sections 1–9 and 12, with mean active widths below this threshold, demonstrate a strong linear relationship between mean active width and variability. Sections 10 and 11, with predominantly larger active widths, appear as scattered outliers with significantly higher variability. Section 10 is affected by anthropogenic influences related to the Pradella Dam, while Section 11 exhibits high erosivity and braiding, both representing morphodynamically active reaches (see Section 6.2.3). Increased variability in these sections is also an indicator of increased morphological activity.

Given the relevance of active width for river corridor delineation and riparian buffer areas, the observed relationship can serve as a preliminary guideline for estimating management zones in homogeneous river reaches. Sections with particularly large active widths require additional attention in management planning. However, it should be noted that this relationship may vary between river systems, and further studies are required to validate these results and investigate the underlying mechanisms across rivers from different contexts.

Scaling Relationship Between Active Width Variability and Taylor Microscale

The scaling relationship between active width variability and spatial autocorrelation scale (Taylor microscale) is presented in Figure 5.11. The Taylor microscale represents the spatial length over which fluctuations in active width remain correlated, while variability (half the 16th–84th percentile range) quantifies the magnitude of these fluctuations. Comparison of these metrics within individual river sections provides insight into both the intensity and persistence of changes in active width.

Figure 5.11 demonstrates that sections with higher variability also exhibit longer Taylor microscale, which can be observed in the moderately confined and highly erosive section 11. This suggests that in such reaches, disturbances can generate substantial and persistent changes in active width that propagate over longer distances. In contrast, valley-confined sections with resistant lithology (e.g., sections 2 and 3) exhibit low variability and short Taylor microscales, indicating more localized and contained fluctuation.

Therefore, Figure 5.11 illustrates levels of longitudinal connectivity and active width variability in homogeneous river sections, which can support river management through identifying zones more vulnerable or resilient to disturbance longitudinal propagation. This framework allows for a more detailed estimation of the spatial influence of river management practice. Management interventions in reaches with high variability and long Taylor microscale are likely to have broader effects. However, these results are specific to the study reach, and additional research is needed to test the generality of these findings across different fluvial contexts and river types.

Comparison of River Active Width and Bottom Width

Figure 5.12 presents a direct comparison between BAFU-measured bottom width at each cross section and the active width extracted from aerial imagery during the 2010s. Comparison results for bottom width measurements in the 2000s and 2020s are provided in Appendix A.9. Both active width and bottom width show similar spatial patterns along the study reach, reflecting the influence of shared geomorphic controls such as lithology and valley confinement. This consistency supports the reliability of the extracted active width.

Generally, the active width exceeds the bottom width at most cross sections, as expected since active width encompasses the full zone of sediment mobility and morphological activity. However, a few cross sections show larger bottom width values, which may be attributed to differences in spatial resolution between the datasets. Additionally, aerial imagery may be captured during low-flow periods, leading to an underestimation of active width. Despite these exceptions, the sectional-averaged bottom width is consistently smaller than the active width, as shown in Figure 5.13.

Figure 5.13 compares temporal trends of section-averaged bottom width and active width. Unlike active width, which is changing over time, bottom width remains relatively stable. This is expected, as active width responds to lateral fluvial processes and sediment dynamics over the riverbanks, which are not reflected by bottom width alone. Most drivers that influence active width, such as flooding, do not affect the bottom width unless significant channel incision or narrowing occurs.

In summary, while active width and bottom width display similar longitudinal trends due to shared geomorphic controls, the active width is more responsive to fluvial dynamics, whereas bottom width generally remains stable over time. Further investigation of the factors influencing bottom width variability could help clarify the differing responses and mechanisms behind these two channel metrics.

6.3 Sediment Dynamics

6.3.1 Flow Regime Characterization via Froude Number—1D Modeling

The longitudinal variation in Froude number in Figure 5.14 offers an insight into the river's hydraulic regime and validates the river segmentation as in Table 5.1. High Froude numbers align with steeper sections, reflecting higher velocities and a greater likelihood of supercritical flow conditions. Conversely, segments with lower slopes exhibit lower Froude numbers, indicating subcritical flow regimes.

For cross sections where external discharges (from tributaries or EKW return flows) enter, Figure 5.14 demonstrates abrupt drops in Froude number, suggesting an increase in depth and a modest rise in velocity. Both gravel-mining sites show sudden decreases in Froude number. The gravel-mining could be reflected in the cross-sectional geometry with a deepened riverbed, leading to an increased flow depth and lower Froude number. The cross sections near the Pradella dam also show an obvious decrease in the Froude number due to the increase of water depth and reduced flow velocity. As a result, localized hydraulic effects can capture the influence of the external discharges, gravel-mining, and Pradella dam.

6.3.2 Bedload Transport and Shear Stress—1D Modeling

Figure 5.15 presents the expected values of the sediment transport ratio (Q_b/Q) calculated using various sediment transport formulas, all of which exhibit similar overall trends along the river. Among them, the formula by Wilcock and Crowe (2003) predicts the highest sediment transport efficiency. This is likely due to its incorporation of the mixing GSD, which includes finer sediments that are more easily mobilized. Although all formulas show similar trends, comparing the calculated results with measured bedload transport data would help validate their accuracy and strengthen the basis for further analysis. Given the varying characteristics of the river sections, it is possible that different formulas may be more suitable for different parts of the river.

The 1D modeling results and post-processed sediment transport rates are based on corrected daily PREVAH-simulated discharges. However, the use of daily averages can smooth out short-duration flood peaks that are critical for activating sediment transport processes. Figure 5.16 compares shear stress estimates derived from model simulations with those calculated using BAFU-measured hourly discharge and water surface elevation (wse) data at cross sections of Cinuos-chel, Tarasp, and Martina.

At Cinuos-chel, the range of hourly-calculated shear stress values is unexpectedly narrower than that of the modeled results. This discrepancy is likely related to an overestimation of the corrected PREVAH-discharge, as discussed in Section 3.3.4. As for Tarasp, the shear stress ranges from both the hourly data and daily model results are similar, suggesting that the daily-resolution model adequately captures flow conditions relevant for sediment transport. At Martina, the hourly data exhibit a much broader range than the daily estimates. This difference may be attributed to the anthropogenic water return pattern at the Martina restitution (see Figure A.5). The daily model output fails to capture these short-term variations, meaning that sediment transport rates derived from the model do not fully reflect the influence of these water returns on bedload transport and potential channel adjustments after Martina restitution.

In summary, while shear stress is overestimated at the upstream end (Cinuos-chel) and underestimated at the downstream end (Martina), leading to corresponding over- and underestimations of sediment transport, the good agreement at Tarasp suggests that the daily simulated discharge provides a reasonable representation of actual conditions across much of the study reach, despite its coarse temporal resolution. Therefore, for locations affected by rapid discharge changes, higher temporal resolution data or modeling are recommended to accurately assess sediment transport and river morphology dynamics.

6.3.3 Riverbed Changes: Model vs. BAFU Measurements

Figure 5.17 presents a comparison between the bed change rates in the 2010s estimated by modeling and the measured bed elevation changes during 2000s–2010s and 2010s–2020s. The estimates from modelling are based on river flow regimes and geometry from the 2010s, providing critical insight into the erosional and depositional dynamics.

In both comparison plots shown in Figure 5.17, there is a substantial discrepancy between the magnitudes on the left and right axes, indicating a significant difference between modeled and measured riverbed changes. One primary reason for the overestimation of erosion and deposition rates in the modeling results may be the neglect of sediment supply limitations. The calculation of sediment transport and subsequent bed level changes was performed under the assumption of unlimited sediment supply, which does not reflect actual conditions in most reaches of the Inn River. In reality, sediment supply is constrained by few tributaries and limited contributions from debris flows. Additionally, the modeling assumed consistent cross-sectional geometry throughout the 2008–2017 period. Since only a hydraulic model was applied without dynamic morphological updating, this approach fails to capture feedbacks from ongoing changes in channel form that would affect subsequent bedload transport and deposition patterns. This oversimplification of static geometry and long-term discharge data may contribute to the discrepancies. Furthermore, both the modeling and measurement approaches may suffer from coarse spatial resolution between cross sections, potentially missing important local morphological changes and leading to discrepancies when comparing reach-averaged results. Given current methodological limitations, these comparisons should primarily be used to assess general trends rather than for precise quantitative analysis. This approach can only provide insights into the relative behavior of different river sections.

To validate the modeling estimates, measured bed elevation changes from the 2010s to 2020s were analyzed and compared with model estimation. In general, the observed bed changes align well with the modeled trends of erosion and deposition, particularly in the river reach downstream of the Pradella dam where multiple sediment sources contribute to a relatively higher sediment supply. In these sections, the modeling effectively captures the measured bed change patterns as dominated aggradation processes. Additionally, at cross sections located near tributary confluences, the river tends to show localized erosion followed by deposition, consistent with both the models and the measurements, except for the tributary immediately upstream of the Pradella dam, where the measured data indicate a sudden deposition, contrary to model predictions. It could be a continuous effect from the Pradella dam. Because the reach upstream of the Pradella dam also exhibits a marked discrepancy between the modeled and measured trends: the model predicts switching between aggradation and erosion, while measurements reveal extended upstream aggradation. This is likely due to sediment being trapped behind

the dam and a reduction in flow velocity, which decreases the sediment transport capacity and promotes deposition. The model may fail to accurately capture the upstream influence of the dam due to an underestimation of the dam's configuration and its effects. Gravel mining activities also influence riverbed dynamics. Both cross sections with active gravel extraction show sudden deposition in measurements, whereas the model predicts erosion. This contrast may be explained by a reduction in gravel extraction activity during the 2010s–2020s in Zernez and Ramosch (see Figure 5.8), which would decrease sediment removal and allow for localized deposition. Human interventions strongly influence sediment erosion and deposition, which may lead to the model's inability to capture such detailed changes. These findings indicate that the modeling approach does not fully capture sediment dynamics upstream of the dam and at gravel mining sites. However, the model performs well in reaches with sufficient sediment supply and less external interventions, accurately reflecting the general trends of erosion and deposition.

When comparing the model with measured changes from 2000s–2010s, the upper river reach shows less erosion or aggradation in the measurements than estimated by the model. This can be attributed to limited sediment supply and a likely overestimation of shear stress in the modeling (see Figure 5.16). The patterns at cross sections influenced by gravel mining and most tributaries remain consistent with the trends observed from 2010s–2020s, suggesting stable external driving factors in these areas. However, a significant exception is found upstream of the Pradella dam, where pronounced measured erosion contrasts with the model's predictions of ongoing deposition. This discrepancy may be due to human interventions for removing accumulated sediment upstream of the dam, altering the expected riverbed response.

In the reaches without measured data shown in Figure 5.17, the model produces relatively high estimated rates of erosion and deposition. A plausible explanation for these intensive estimated riverbed changes is the potential underestimation of representative grain size (d_s). As discussed in Section 3.4, this river segment near Ardez is characterized by pronounced armoring, where a layer of coarse surface grains protects finer bed sediment from mobilization. However, the sediment transport calculations use the combined GSD, thereby implying mobility of both surface and substrate material over decadal timescales. In reality, due to strong armoring, the fine substrate is likely to remain immobile even during the analyzed 10-year period. Including substrate sediment in transport calculations may therefore overestimate both sediment transport rates and the resulting intensity of bed erosion and aggradation.

Based on the identified limitations, several recommendations can enhance future studies of riverbed evolution along the Inn River. Future modeling frameworks should explicitly incorporate sediment supply constraints, either by limiting transport calculations or by integrating observed supply data. It is also advisable to use morphodynamic models that account for feedback between changing bed geometry and sediment transport processes. Increasing the spatial resolution of model predictions for localized comparison with field measurements would allow for more accurate capture of morphological changes. This approach helps reduce the smoothing effects caused by spatial averaging. The impact of human interventions, such as gravel mining, should be incorporated into the models by introducing local sediment sinks to accurately represent their influence on sediment dynamics. Additionally, the dam configuration should be validated to ensure its effects are properly captured in the simulations. Further validation of the GSD used in sediment transport calculations across the simulation periods is also recommended.

7 Conclusions

This study analyzed channel changes and their external driving forces along the Inn River, combining evolutionary trajectory analysis with sediment dynamics modeling to support effective river management strategies.

Evolutionary Trajectories

River characterization and segmentation revealed distinct sections with similar morphological trends and drivers. However, historical variability from natural events and human interventions may have compromised this assumption, underscoring the need to integrate historical river characteristics for improved analysis. Active width trajectories emphasized the importance of temporal resolution, as high-frequency narrowing–widening cycles and other short-term changes could be missed due to gaps in aerial imagery, highlighting the necessity for high-resolution temporal datasets to better capture these dynamics and inform management. Furthermore, morphological processes occurred at different spatial scales: While centerline migration and active width changes occurred across multiple sections, bar dynamics, braiding, and avulsion were limited to specific reaches, necessitating management strategies that consider both local and reach-scale drivers.

Evolutionary trajectory analysis in a global view showed that active width and centerline migration followed coherent longitudinal trends driven by flood dynamics. Prolonged low-flood periods led to channel narrowing through bank stabilization and sediment deposition, while high-magnitude floods caused widening, with extreme events potentially triggering irreversible morphological changes. However, centerline dynamics were also shaped by asymmetric bank erosion, sedimentation, and human confinement (e.g., levees, embankments). Future studies should employ process-based riverbank erosion models incorporating bank material, planform curvature, and human interventions to better predict centerline evolution.

Sectional analyses of evolutionary trajectories, particularly in sections 5 and 11, revealed the interplay between sediment supply, gravel extraction, and sediment transport, which drove bar morphology, channel braiding, and avulsion of flow path. Dam construction in section 10 altered sediment budgets, disrupting downstream sediment continuity. Future studies should quantitatively evaluate sediment budget components to better understand these interactions.

Exploration of active width for river management

The relationship between active width and its variability helped identify fluvially influenced zones in homogeneous sections, while comparisons with the Taylor microscale guided river management by highlighting zones that were more vulnerable or resilient to disturbance propagation. These insights should be tested in other fluvial systems to evaluate their generality and underlying mechanisms. Although active and bottom widths shared similar longitudinal trends due to common geomorphic controls, active width was more responsive to fluvial dynamics over time, whereas bottom width remained relatively stable. Further investigation of bottom width variability is recommended to better understand their different responses.

Sediment dynamics

Sediment dynamics evaluated with 1D hydraulic simulations indicated that daily PREVAH-simulated discharge reasonably represented overall conditions, though shear stress tended to be

slightly overestimated near the river's upper part and underestimated toward its downstream end. Higher temporal resolution data or modeling is recommended to better capture discharge peaks and sediment transport dynamics.

The model effectively captured sediment dynamics in areas with sufficient sediment supply and limited external drivers but performed poorly upstream of the dam and in gravel-mining zones. Future modeling should incorporate sediment supply constraints and observed sediment supply data, use morphodynamic models with bed-geometry feedback, and increase spatial resolution to reduce averaging effects over 150 m on riverbed change estimation. Dam configurations and sediment trapping must be validated, while human interventions like gravel mining should be represented through local sediment sinks. Further validation of grain-size distributions (GSD) across simulation periods is also recommended.

8 Acknowledgment

I would like to express my sincere gratitude to Ludovico Agostini for his weekly guidance and for providing the initial idea that shaped this thesis. His continuous support and insightful feedback have been invaluable throughout this journey. I am also deeply thankful to Professor Peter Molnar for his valuable suggestions and thoughtful input during the research process, which greatly contributed to the development of this work. Additionally, I acknowledge the use of OpenAI's ChatGPT for assistance with language polishing and improving the clarity of the manuscript.

Bibliography

Abderhalden, A. et al. (2016). Landschaftsqualitätsprojekt kanton graubünden engiadina bassa, samnaun, val müstair: Projektbericht stand 2016. Technical report, Arinas environment AG, Chur, Switzerland. Project report.

Anastasi, G. (1984). Geschiebeanalysen im felde unter berücksichtigung von grobkomponenten. *Mitteilungen der Versuchsanstalt für Wasserbau, Hydrologie und Glaziologie an der Eidgenössischen Technischen Hochschule Zürich*, 70.

BAFU (2016). *NADUF:National Long-Term Surveillance of Swiss Rivers*. BAFU, eawag. `www.naduf.ch`.

Brierley, G. and Fryirs, K. (2009). Don't Fight the Site: Three Geomorphic Considerations in Catchment-Scale River Rehabilitation Planning. *Environmental Management*, 43(6):1201–1218.

Center, H. E. (2022). *HEC-RAS River Analysis System*. U.S. Army Corps of Engineers.

Church, M. (2006). BED MATERIAL TRANSPORT AND THE MORPHOLOGY OF ALLUVIAL RIVER CHANNELS. *Annual Review of Earth and Planetary Sciences*, 34(1):325–354.

Egger, G., Abderhalden, A., Herrmann, T., and Muhar, A. (2019). Inn. In Muhar, S., Muhar, A., Gregory, E., and Siegrist, D., editors, *River of the Alps. Diversity in Nature and Culture*, pages 404–407. HAUPT, Bern, Switzerland.

Engadiner Kraftwerke AG (2025). Anlagenschema. Accessed: 2025-07-02.

ETH Zurich, VAW (2024). *BASEMENT – Basic Simulation Environment for Computation of Environmental Flows and Natural Hazard Simulation, Version 4.1.0*. ETH Zurich, Laboratory of Hydraulics, Hydrology and Glaciology (VAW). Software documentation.

Federal Office of Topography swisstopo (2025). Journey through time – aerial images. © swisstopo, 2025. Accessed 2025-07-02.

Haas, F., Heckmann, T., Wichmann, V., and Becht, M. (2004). Change of fluvial sediment transport rates after a high magnitude debris flow event in a drainage basin in the Northern Limestone Alps, Germany. *Tunnelling and Underground Space Technology*, 15(2):13.

Hashemi, S., Carrivick, J., and Klaar, M. (2023). Hydromorphological response of heavily modified rivers to flood releases from reservoirs: A case study of the Spöl River, Switzerland. *Earth Surface Processes and Landforms*, 49(3):1028–1046.

Kevic, M., Ortlepp, J., Mürle, U., and Robinson, C. (2018). Effects of experimental floods in two rivers with contrasting valley morphologies. *Fundamental and Applied Limnology / Archiv für Hydrobiologie*, 2:145–160.

Kondolf, G. M. (1994). Geomorphic and environmental effects of instream gravel mining. *Landscape and Urban Planning*, 28(2-3):225–243.

Legates, D. R. and McCabe, G. J. (1999). Evaluating the use of "goodness-of-fit" measures in hydrologic and hydroclimatic model validation. *Water Resources Research*, 35(1):233–241.

Massong, T. M. and Montgomery, D. R. (1999). Preliminary analysis of median grain size and armoring comparisons from field studies in oregon and washington. Technical report, U.S. Forest Service Stream Team, 4812 Osuna Pl. NE, Albuquerque, NM 87111 and Department of Geological Sciences, University of Washington, Seattle, WA 98195. Prepared for the U.S. Forest Service Stream Team.

Meyer-Peter, E. and Müller, R. (1948). Formulas for bed-load transport. *Proc., 2nd Meeting*, IAHR, Stockholm, Sweden:39–64.

Nash, J. and Sutcliffe, J. (1970). River flow forecasting through conceptual models part i — a discussion of principles. *Journal of Hydrology*, 10(3):282–290.

Parker, G. (1979). Hydraulic geometry of active gravel rivers. *Journal of the Hydraulics Division, ASCE*, 105(9):1185–1201.

Parker, G. (1990). Surface-based bedload transport relation for gravel rivers. *Journal of Hydraulic Research*, 28(4):417–436.

Parker, G., Klingeman, P. C., and McLean, D. G. (1982). Bedload and size distribution in paved gravel-bed streams. *Journal of the Hydraulics Division, ASCE*, 108(4):544–571.

Recking, A. (2013). A simple method for calculating reach-averaged bedload transport. *Journal of Hydraulic Engineering*, 139(1):70–75.

Redolfi, M., Tubino, M., Bertoldi, W., and Brasington, J. (2016). Analysis of reach-scale elevation distribution in braided rivers: Definition of a new morphologic indicator and estimation of mean quantities. *Water Resources Research*, 52(8):5951–5970.

R.E.Glover, Q. (1951). *Stable Channel Profiles*. Design and Construction Division Engineering Laboratories Branch, Denver, Colorado.

Rickenmann, D. (1991). Hyperconcentrated flow and sediment transport at steep slopes. *Journal of Hydraulic Engineering, ASCE*, 117(11):1419–1439.

Rinaldi, M., Surian, N., Comiti, F., and Bussettini, M. (2015). A methodological framework for hydromorphological assessment, analysis and monitoring (idraim) aimed at promoting integrated river management. *Geomorphology*, 251:122–136.

Robinson, C., Siebers, A., and Ortlepp, J. (2018). Long-term ecological responses of the river spöl to experimental floods. *Freshwater Science*, 37:000–000.

Scorpio, V., Zen, S., Bertoldi, W., Surian, N., Mastronunzio, M., Prá, E. D., Zolezzi, G., and Comiti, F. (2017). Channelization of a large Alpine river: what is left of its original morphodynamics? *Earth Surface Processes and Landforms*, 43(5):1044–1062.

Swisstopo (2024a). A journey through time – aerial images. `https://www.swisstopo.admin.ch/en/timetravel-aerial-images`. Accessed 2025-07-02.

Swisstopo (2024b). Swissalti3d height model. `https://www.swisstopo.admin.ch/en/height-model-swissalti3d`. Accessed 2025-07-02.

Ufficio federale dell'ambiente (FOEN/BAFU) (2017). Standard tecnici per la misurazione dei corsi d'acqua. Technical report, FOEN/BAFU. Disponibile online: https://www.bafu.admin.ch/dam/bafu/it/dokumente/naturgefahren/fachinfodaten/flussvermessung.pdf.download.pdf/misurazione$_d$ei$_c$orsidacqua.pdf.

Van Denderen, R. P., Kater, E., Jans, L. H., and Schielen, R. M. (2022). Disentangling changes in the river bed profile: The morphological impact of river interventions in a managed river. *Geomorphology*, 408:108244.

Viviroli, D., Zappa, M., Gurtz, J., and Weingartner, R. (2009). An introduction to the hydrological modelling system PREVAH and its pre- and post-processing-tools. *Environmental Modelling Software*, 24(10):1209–1222.

Wilcock, P. R. and Crowe, J. C. (2003). Surface-based transport model for mixed-size sediment. *Journal of Hydraulic Engineering*, 129(2):120–128.

Wolman, M. (1954). A method of sampling coarse river-bed material. *Transactions, American Geophysical Union*, 35(6):951–956.

Wong, M. and Parker, G. (2006). Reanalysis and correction of bed-load relation of meyer-peter and müller using their own database. *Journal of Hydraulic Engineering*, 132(11):1159–1168.

List of Symbols for Bedload Transport

Θ = Shields stress (dimensionless)

Θ_c = Critical Shields stress (dimensionless)

d_s = Sediment diameter such that s% of the distribution is finer (m)

φ = Logarithmic grain size scale defined as $\varphi = -\log_2\left(\frac{d}{d_0}\right)$, where d is the particle diameter (mm) and $d_0 = 1\,\text{mm}$ is the reference diameter

i_b = Bed slope

i_E = Energy slope

i = Water surface slope

wse = Water surface elevation (m)

U = Average water velocity across the cross section (m/s)

R_h = Hydraulic radius (m)

K_s = Strickler friction number ($\text{m}^{1/3}/\text{s}$)

w = Water surface width, defined as horizontal distance across the water surface at the cross section (m)

Q = Discharge or flow rate for each cross section (m^3/s)

α = Kinetic energy correction factor

γ = Correction factor accounting for variations in flow velocity across each strip.

Ω = Wetted area for each cross section (m^2)

W = Analyzed cross-sectional width (m)

W_b = Bottom width of cross sections (m)

u_* = Shear velocity (m/s)

g = Gravitational acceleration ($\text{m}\,\text{s}^{-2}$)

q_b = Bedload transport rate per unit width ($\text{kg}\,\text{m}^{-1}\,\text{s}^{-1}$)

Q_b = Bedload transport rate ($\text{m}^3\,\text{s}^{-1}$)

R_h = Hydraulic radius (m)

Φ = Dimensionless bedload transport rate 1 (–)

W^* = Dimensionless bedload transport rate 2 (–)

ϕ_{50} = Normalized Shields stress

τ = Bed shear stress, the force per unit area exerted by flowing water on the bed (Pa or N/m^2)

τ^*_{r50} = Reference shields stress with a value of 0.0876

Δ = Relative submerged density with a value of 1.65 (= (ρ_s - ρ)/ρ)

ρ_s = Density of sediment (typically quartz) = 2650 kg/m^3

ρ = Density of fluid (typically water) = 1000 kg/m^3

Fr = Froude number (dimensionless)

W_j^* = Dimensionless transport rate of partical size fraction j.

d_j = Gometric mean diameter of partical size fraction j

d_{sm} = Geometric mean particle diameter on the bed surface.

τ_{cj} = Critical shear stress of partical size fraction j

τ_r = Reference shear stress

τ_{rj} = Reference shear stress ofpartical size fraction j

τ_{rm} = Reference shear stress of mean size of bed surface

F_j = Proportion of fraction j in surface size distribution

F_s = Proportion of sand in surface size distribution

η = Riverbed elevation (m)

A Appendix

A.1 Calculation of Average Riverbed Bottom Elevation

The average elevation of the riverbed bottom enables monitoring of riverbed evolution.

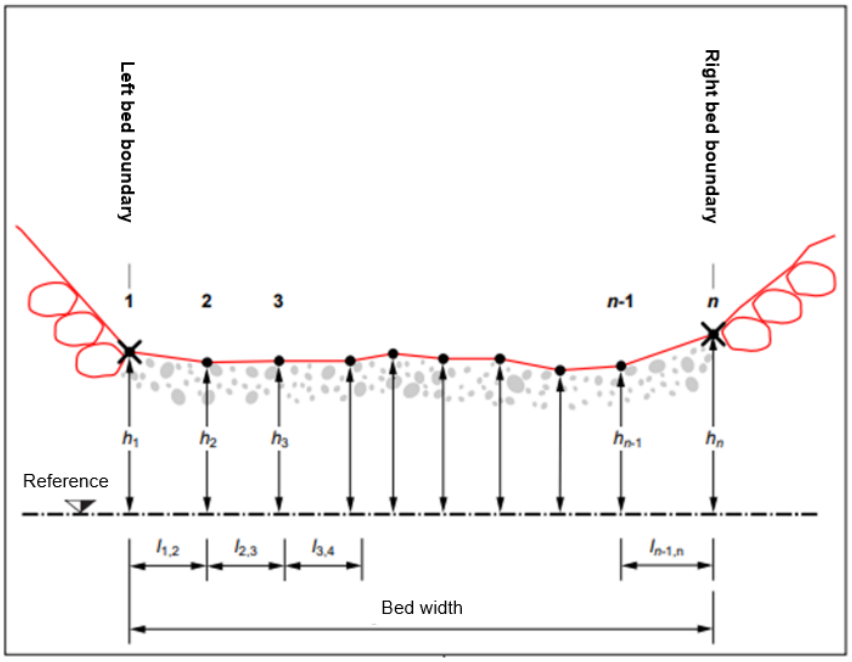

Figure A.1: Indication of measured cross sections from Ufficio federale dell'ambiente (FOEN/BAFU) (2017)

$$\text{Average riverbed bottom elevation} = \frac{\frac{(h_1+h_2)}{2} \cdot l_{1,2} + \frac{(h_2+h_3)}{2} \cdot l_{2,3} + \cdots + \frac{(h_{n-1}+h_n)}{2} \cdot l_{n-1,n}}{l_{1,2} + l_{2,3} + \cdots + l_{n-1,n}} \tag{A.1}$$

where:
- $h_1, h_2, \ldots, h_{n-1}, h_n$ = Elevation of measurement points between the riverbed boundaries (m a.s.l.)
- $l_{1,2}, l_{2,3}, \ldots, l_{n-1,n}$ = Horizontal distance between individual measurement points (m)

A.2 Cross-sectional Data from DEM

350 measured cross-section profiles within the targeted river reach were provided by BAFU in Figure 3.1. However, a 7.125 km segment within this reach lacked cross-sectional measurements. To fill this data gap, cross-sections were generated from DEM data at 150 m intervals using HEC-RAS (Hydrologic Engineering Center's River Analysis System)(Center (2022)). This approach resulted in a total of 398 cross-sections for the entire study reach.

A limitation of DEM-derived cross sections is that they represent only the water surface elevation and do not capture the actual riverbed profile beneath the water surface, which results in an

overestimation of the riverbed elevation. To estimate the elevation difference Δh between the riverbed and the water surface, the cross-sections immediately upstream and downstream of the gap were analyzed. Water surface elevation extracted from the DEM data was compared with the measured bed elevation from BAFU at these locations. The Δh at the two cross-sections are 1.18 m and 1.2 m, respectively. Consequently, a Δh value of 1.19 m was assumed for the gap segment.

To ensure a natural and stable river profile after these adjustments, the DEM-derived cross-sections were further refined using the equilibrium bank model proposed by R.E.Glover (1951).

A.3 NSE and Mean Error

Nash-Sutcliffe Efficiency (NSE) is a statistical measure that evaluates the accuracy of model predictions compared to observed data.

$$NSE = 1 - \frac{\sum_{i=1}^{N}(O_i - P_i)^2}{\sum_{i=1}^{N}(O_i - \bar{O})^2} \tag{A.2}$$

where O_i is the observed value, P_i is the predicted value, $\bar{O}$ is the mean of the observed values, and N is the number of observations. Its range ranges from negative to 1, with a value of 1 indicating a perfect match between observed and predicted values. (Nash and Sutcliffe (1970))

Mean error is a measure of the average difference between model predictions and observations. It indicates whether, on average, the model overestimates or underestimates the observed values.

$$\text{Mean Error} = \frac{1}{N}\sum_{i=1}^{N}(P_i - O_i) \tag{A.3}$$

where P_i is the predicted value, O_i is the observed value, and N is the number of observations. A mean error of 0 indicates a perfect match between observations and predictions (Legates and McCabe (1999)).

Ideally, a model should have a Nash–Sutcliffe Efficiency (NSE) close to 1 and a mean error close to 0 for accurate predictions.

A.4 Correction of PREVAH-simulated Discharge

A.4.1 EKW Operational Rules for Derivations and Restitution

For the derivations, operational patterns were established by analyzing the linear relationship between PREVAH-simulated discharge and EKW-measured water extraction at daily resolution, up to the respective maximum extraction capacities in Table 3.4. Hexagonal binning was applied to the scatter plots, and the centers of the hexagons with the highest point density were selected to fit the linear relationship. The resulting operational rules are presented in Figure A.2a to A.2c for the S-chanf, Clemgia, and Prevah derivations.

Due to the lack of operational data for the Vallember and Varusch derivations, their operational rules were assumed to be analogous to those of Clemgia, given their similar maximum extraction

capacities as indicated in Table 3.4. Accordingly, it was assumed that 70% of the natural tributary flow can be extracted for Vallember and Varusch, up to their respective maximum capacities of 5 and 5.2 m^3/s.

For the Martina restitution, Figure A.2d shows the daily restitution discharges, which were generated by randomly sampling values for each day of the year based on the mean and standard deviation derived from seven years of operational data. This water release rule is applicable only for the period after 1994 due to the operational pattern change in 1993.

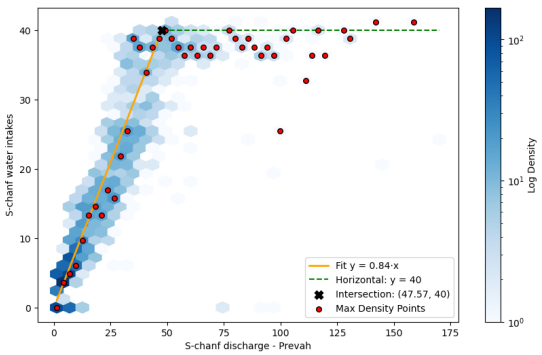

(a) S-chanf derivation

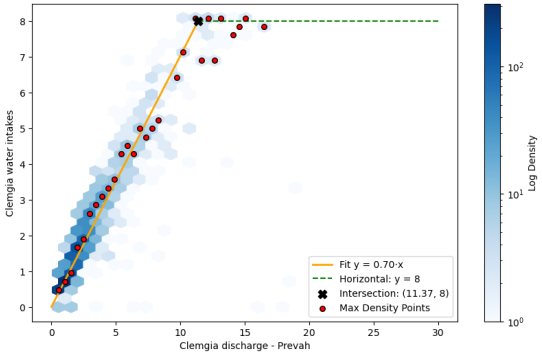

(b) Clemgia derivation

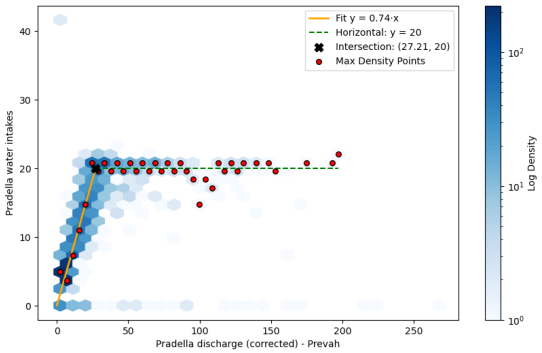

(c) Pradella derivation

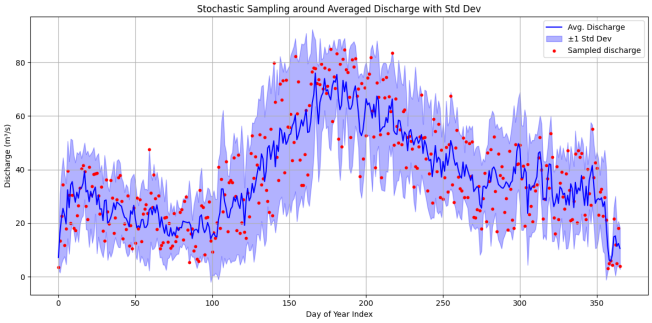

(d) Martina restitution

Figure A.2: EKW operational rules for (a) S-chanf, (b) Clemgia, (c) Pradella, and (d) Martina

Based on the established operational rules, the PREVAH-simulated discharge was corrected to account for EKW water redistribution. To validate these corrected discharge values, comparisons were made between the corrected PREVAH simulations and BAFU-measured discharge at four locations within the study area, using two different evaluation methods.

A.4.2 Validation: NSE and Mean Error

The first validation method involved a direct comparison of the corrected PREVAH-simulated discharge with the BAFU-measured discharge at daily resolution. To ensure consistency, the BAFU-measured data, originally recorded at hourly or 5-minute intervals, was averaged to obtain daily values. The agreement between the two time series was assessed using the NSE and mean error metrics. The validation results, including the NSE and mean error values, are presented in Figure A.3.

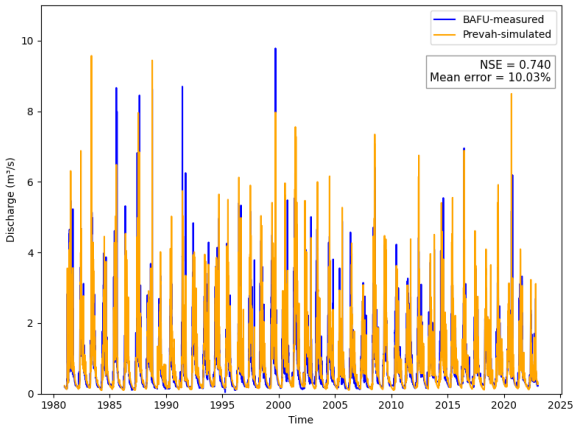

(a) Cluozza

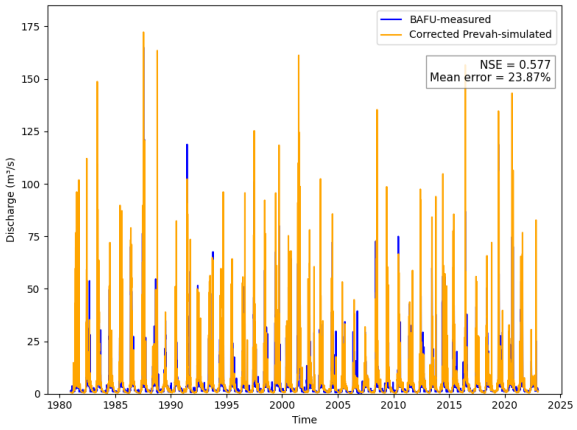

(b) Cinuos-chel

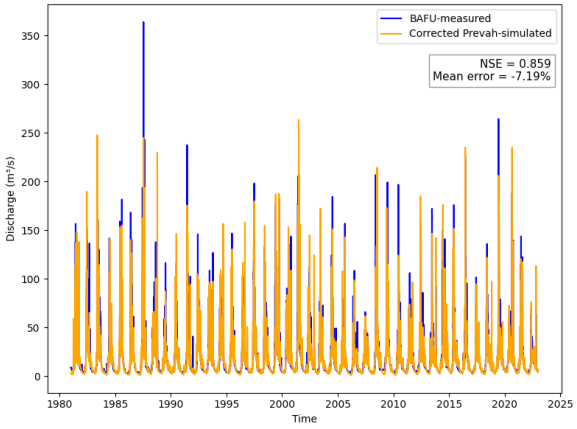

(c) Tarasp

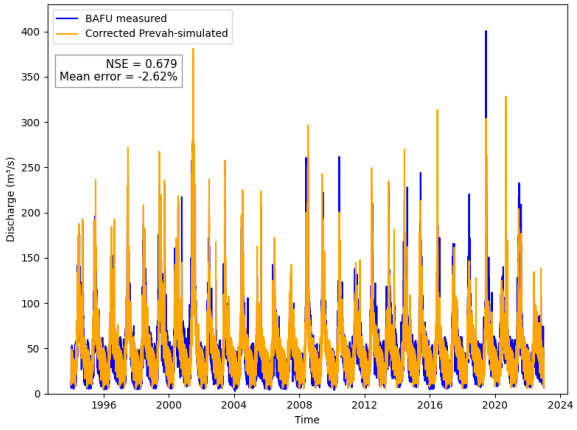

(d) Martina

Figure A.3: Validation of corrected PREVAH-simulated discharge based on NSE and mean error at four gauging stations: (a) Cluozza, (b) Cinuos-chel, (c) Tarasp, and (d) Martina

A.4.3 Validation: Distribution Analysis of the Residuals

The second method to assess the agreement between the PREVAH-simulated and BAFU-measured values is to calculate the differences (residuals) for each data point as follows:

$$d_i = P_j - O_i \tag{A.4}$$

where P_j represents the predicted value (PREVAH-simulated discharge at daily resolution), O_i is the observed value (BAFU-measured discharge at hourly or 5-minute intervals), and d_i is the difference (residual) for each observation$i$.

This method assesses the deviation of high-frequency measured discharge from the simulated daily discharge. To facilitate comparison across different locations, each residual was normalized by the channel width, as measured from 2021 Swisstopo aerial imagery, resulting in unit discharge residuals. The distribution of these normalized residuals was analyzed using probability histograms and descriptive statistics, including the mean, standard deviation, skewness, and excess kurtosis. The validation results are shown in Figure A.4.

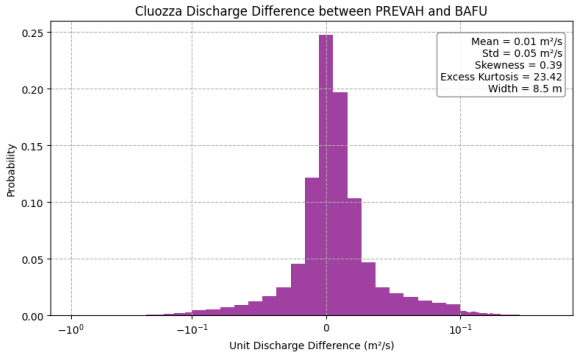

(a) Cluozza

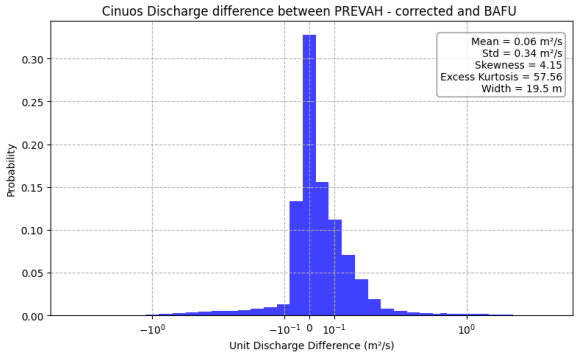

(b) Cinuos-chel

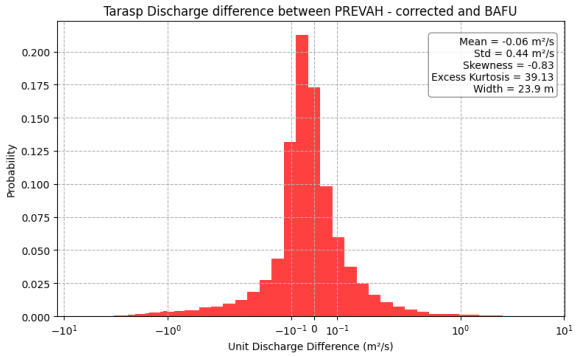

(c) Tarasp

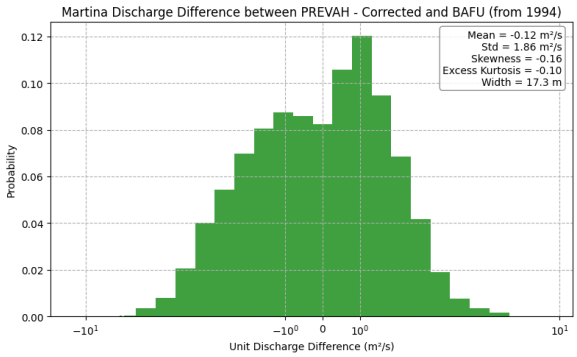

(d) Martina

Figure A.4: Validation of corrected PREVAH-simulated discharge based on distribution of residuals (differences) at four gauging stations: (a) Cluozza, (b) Cinuos-chel, (c) Tarasp, and (d) Martina

The Cluozza gauging station serves as a reference for evaluating the performance of PREVAH simulation, as it is unaffected by EKW interventions. As shown in Figure A.4, the mean residuals at all four gauging stations range from –0.12 to 0.06 m^2/s, indicating minimal systematic bias across the study area. However, the standard deviation (std) of the residuals increases progressively from upstream to downstream (Cinuos-chel, Tarasp, and Martina), reflecting the cumulative impact of EKW interventions incorporated into the PREVAH-simulated discharge. This bias likely results from the oversimplification of the EKW operational rules, leading to the accumulation of modification errors in downstream reaches. Regarding the distributional skewness, only the Cinuos-chel location exhibits pronounced right skewness. This may be attributed to the three derivations upstream, which have a combined maximum capacity of 50.2 m^3/s, with two lacking actual operational data. The assumed operational rules for the Vallember and Varusch derivations may not accurately reflect real extraction patterns, as they might extract more than the assumed 70% of incoming flow before reaching maximum capacity. Excess kurtosis, which quantifies the heaviness of the tails relative to a normal distribution, also varies among stations. The histograms for Cluozza, Cinuos-chel, and Tarasp display excess kurtosis values exceeding 20, indicative of distributions with heavy tails and sharp peaks. In contrast, the Martina station shows an excess kurtosis value near zero, corresponding to a distribution with lighter tails and a flatter peak. This difference is likely due to the highly regulated release pattern at Martina, where restitution discharges exhibit a rectangular shape with abrupt increases and decreases (see Figure A.5). Such a release regime results in a residual distribution

characterized by a flatter peak and lighter tails.

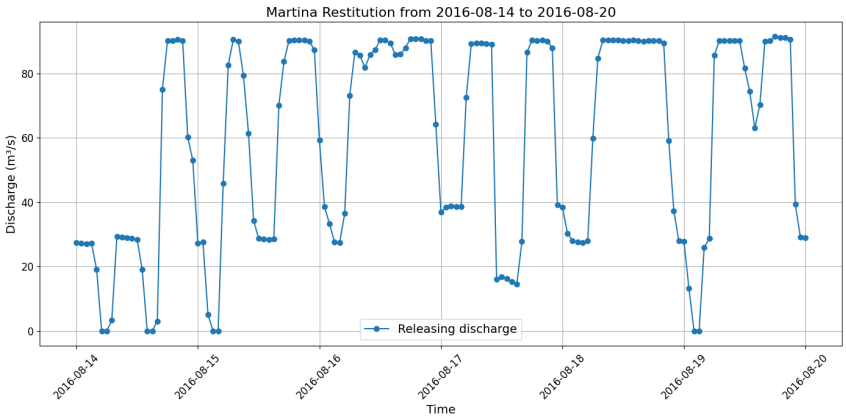

Figure A.5: Example of releasing water pattern in Martin restitution

A.4.4 Comparison of Two Validation Methods

The validation results presented in Figures A.3 and A.4 provide different perspectives on the model and modification performance. While the NSE and mean error metrics offer a direct assessment of agreement between the corrected PREVAH-simulated and BAFU-measured daily discharges, the residual distribution analysis accounts for differences in temporal resolution, highlighting the loss of detail inherent to daily-averaged data. This limitation is particularly evident at the Martina restitution site, where daily discharge values may not adequately capture the daily variability of water releases (see Figure A.5).

The implications of discharge resolution for bedload transport calculations are shown in Section 5.5.2 through shear stress. Given these considerations, the use of NSE and mean error metrics based on daily discharge comparisons is sufficient for validation, as they provide a clear and direct assessment of model accuracy, including the degree of agreement and any tendencies toward over- or underestimation.

A.5 Surface and Subsurface GSD

The subsurface and surface GSD of the sampling locations are shown in Figure A.6 and A.7. Figure 3.3 indicates the sampling locations in the study area.

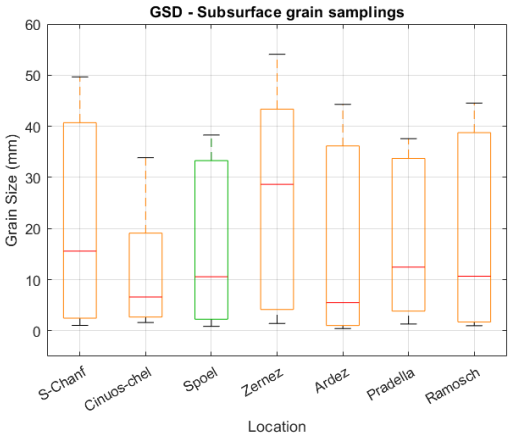

Figure A.6: Subsurface GSD of the sampling locations

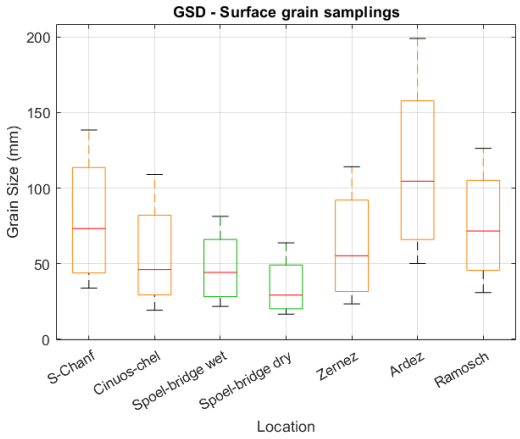

Figure A.7: Surface GSD of the sampling locations

A.6 Estimation of Positional Uncertainty in Active Width

According to the workflow in Section 4.1.2, the positional uncertainty in defining the active width of the river was primarily related to the resolution of the aerial images and the smoothing of the bankline. The hand-drawn error was considered negligible. For aerial image resolution, the left and right banklines were treated as uncorrelated, and their combined uncertainty was calculated using Equation (A.5):

$$\sigma_{\text{resolution}} = \sqrt{\sigma_{\text{left}}^2 + \sigma_{\text{right}}^2} \tag{A.5}$$

where σ_{left} and σ_{right} are the uncertainties of the left and right banklines, respectively.

Based on the image resolution values provided in Table 3.1, the calculated resolution uncertainty was 0.1414 m for 1946, 0.717 m for 1956–2002, 0.3536 m for 2005–2014, and 0.141 m for 2018 and 2021.

The uncertainty from bankline smoothing was quantified by calculating the area difference between the hand-drawn and the smoothed banklines, normalized by the average length of the two corresponding lines. For each bankline and survey year, this measure represented the average lateral discrepancy introduced by the smoothing process. The Root Mean Square Error (RMSE) was then used to evaluate the average smoothing uncertainty across all 16 surveyed years, as shown in Equation (A.6):

$$\text{RMSE} = \sqrt{\frac{1}{N}\sum_{i=1}^{N}\left(\Delta_{\text{smoothed}}(i)\right)^2} \tag{A.6}$$

where $\Delta_{\text{smoothed}}(i)$ denotes the smoothing uncertainty calculated for the i-th survey year, and $N = 16$ is the number of survey years. As the left and right banklines were independent, the total smoothing uncertainty was calculated by combining their respective RMSE values using Equation (A.7):

$$\sigma_{\text{smooth}} = \sqrt{\text{RMSEleft}^2 + \text{RMSEright}^2} \tag{A.7}$$

This yielded a smoothing uncertainty of 0.0991 m.

To determine the overall positional uncertainty in each surveyed year, the combined effects of

aerial image resolution and bankline smoothing were considered using Equation (A.8):

$$\sigma_{\text{sum}} = \sqrt{\sigma^2_{\text{resolution}} + \sigma^2_{\text{smooth}}} \tag{A.8}$$

This aggregated uncertainty was used in the subsequent analysis of active width evolution. In particular, all active width values were normalized to the initial measurement in 1946, and the difference in normalized active width between consecutive surveyed years was analyzed to detect periods of widening, narrowing, or stability. The propagated uncertainty associated with each difference was calculated using Equation (A.9):

$$\epsilon_\Delta(i) = \left| \frac{W_{i+1} - W_i}{W_{1946}} \right| \cdot \sqrt{\frac{\sigma^2_{i+1} + \sigma^2_i}{(W_{i+1} - W_i)^2} + \frac{\sigma^2_{1946}}{W^2_{1946}}} \tag{A.9}$$

where W_i and σ_i denote the active width and its associated uncertainty for the i-th year, and W_{1946} and σ_{1946} correspond to the active width and its associated uncertainty in 1946. This formulation ensured that uncertainty propagation was rigorously accounted for in both the measured change and its normalization, providing a reliable basis for assessing the statistical significance of observed active width changes. If the computed change exceeded the propagated uncertainty, it was considered a period of narrowing or widening; otherwise, the period was classified as stable within the margin of uncertainty.

A.7 BAFU-measured Discharge for the External Forcings

Figure A.8 presents the annual flood durations (expressed as the number of flooding days per year) alongside the maximum discharge recorded in each flood year, based on BAFU-measured data. Flooding days were defined as days when the discharge exceeded the 99th percentile at all three Inn River gauging stations (Cinuos-chel, Tarasp, and Martina). For each year with flooding days, the maximum discharge was taken as a measure of flood intensity. The figure illustrates flood intensity as observed at all three stations, and although the absolute magnitudes differed substantially between stations, the ranking of flood intensity across years was relatively similar throughout the river. Since the analysis of external forcings was concerned primarily with inter-annual variability in relative flood intensity rather than the absolute discharge values, the flood intensity measured at the upstream station Cinuos-chel was considered representative for the entire river reach.

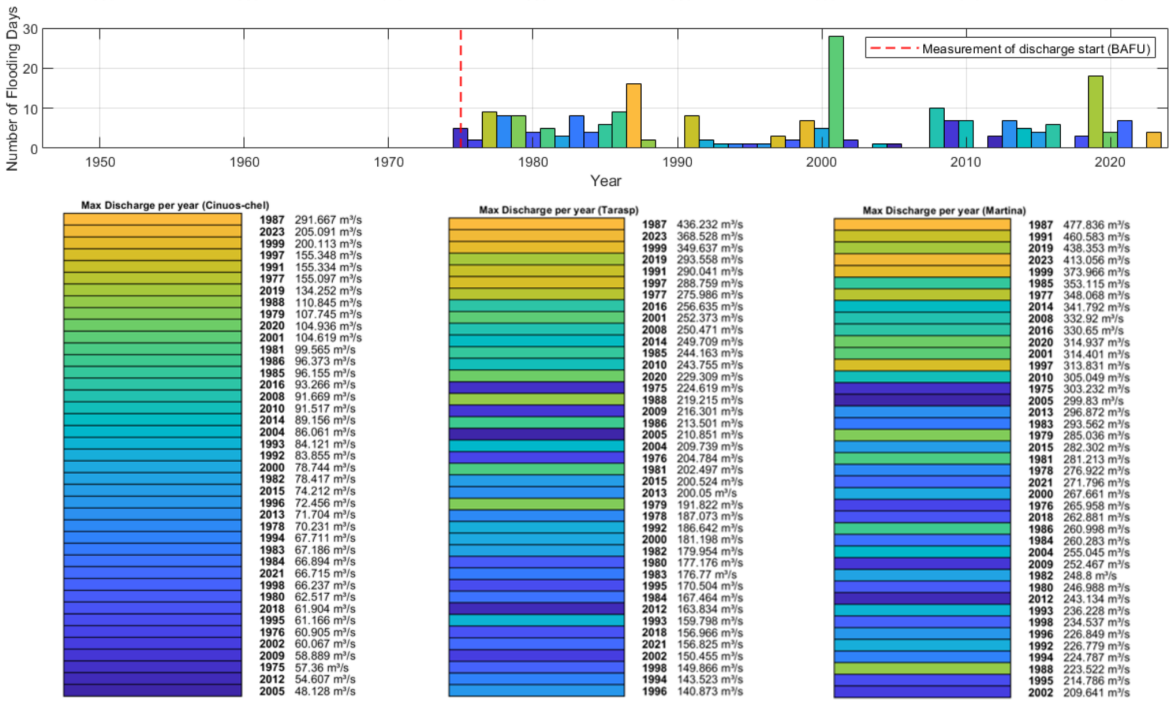

Figure A.8: Flooding duration identified from BAFU-measured discharge with maximum annual discharge at Cinuos-chel, Tarasp, and Martina stations

A.8 Additional Figures for Evolutionary Trajectories—Sectional View

Figure A.9 shows the morphological changes and their associated external forcings in a sectional view.

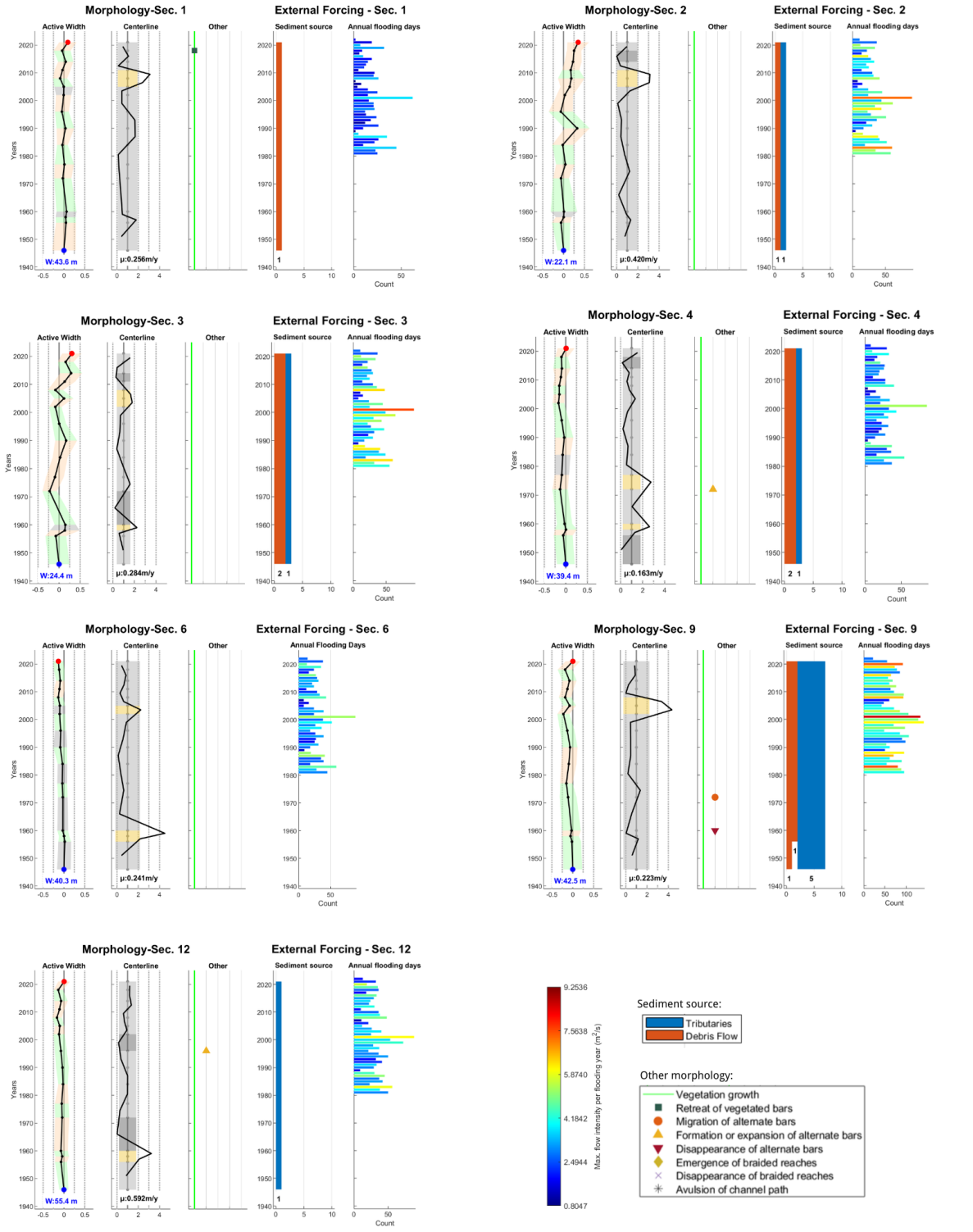

Figure A.9: Evolutionary trajectories of morphological changes and associated external forcings in Sections 1–4, 6, 9, and 12 (W_{blue}: active width in 1946, μ: average centerline migration rate)

A.9 Additional Figures for Longitudinal Comparison between Active Width and Bottom width

Appendix Figures A.10a and A.10b present longitudinal comparisons between the extracted active channel width and the BAFU-measured bottom width along the Inn River for the 2000s and 2020s, respectively.

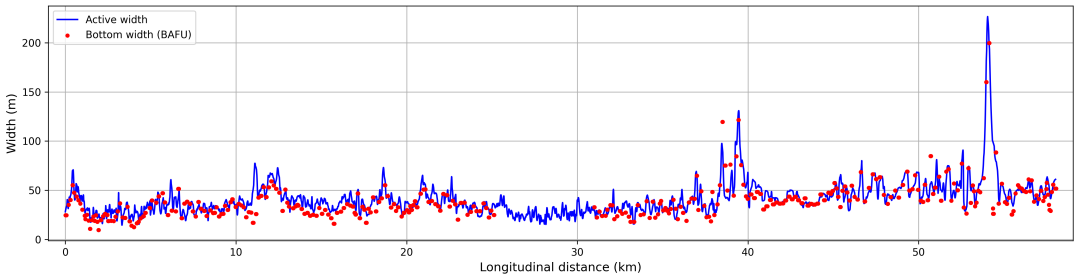

(a) 2000s

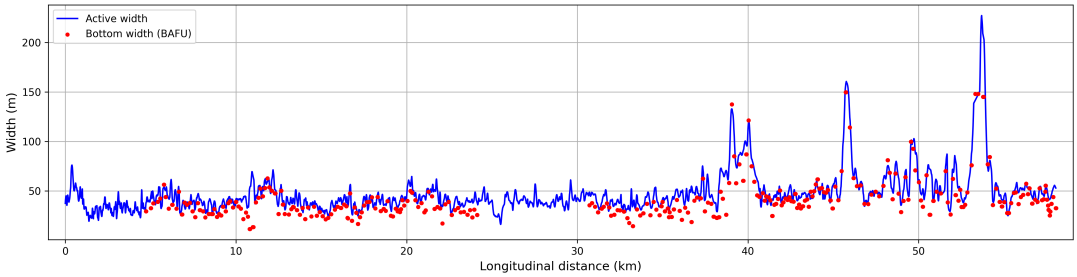

(b) 2020s

Figure A.10: Longitudinal comparisons of active channel width and BAFU-measured bottom width along the Inn River in the 2000s and 2020s.

A.10 Calibrated Strickler Number K_s for Model Setup

Figure A.11 presents two selected high flow events, HF1 and HF2, used for the calibration and validation of friction parameters (Strickler coefficients, K_s). Model performance was assessed by comparing simulated discharges with observed data, using mean absolute error (MAE), Nash-Sutcliffe Efficiency (NSE), and cumulative discharge over each event as evaluation metrics.

After calibrating the 1D hydraulic model with HF1 (see Figure A.12), the K_s values were determined as detailed in Table A.1. Validation results using the HF2 event are illustrated in Figure A.13.

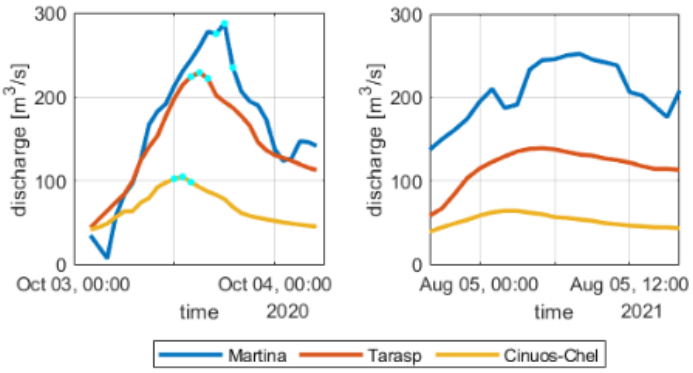

Figure A.11: Selected high flooding (HF) events for strickler number K_s calibration and validation: HF1 (2020-10-03 to 2020-10-04) and HF2 (2021-08-04 to 2021-08-05)

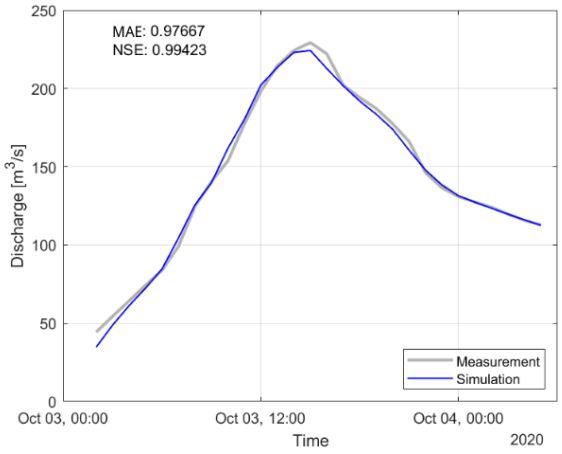

(a) Inn-Tarasp: continuou flow

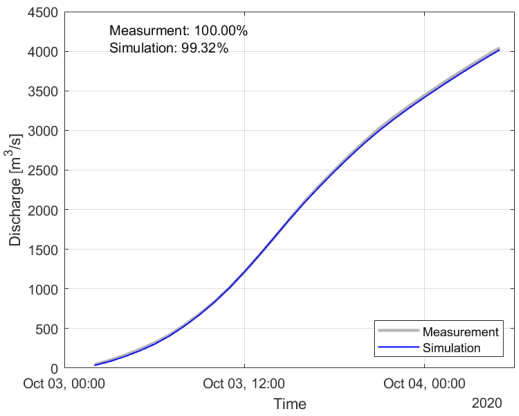

(b) Inn-Tarasp: cumulative flow

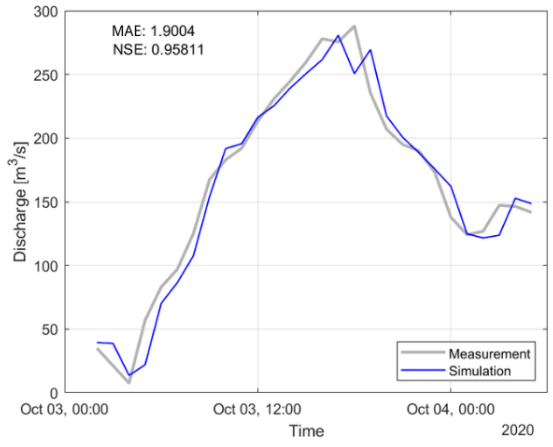

(c) Inn-Martina: continuous flow

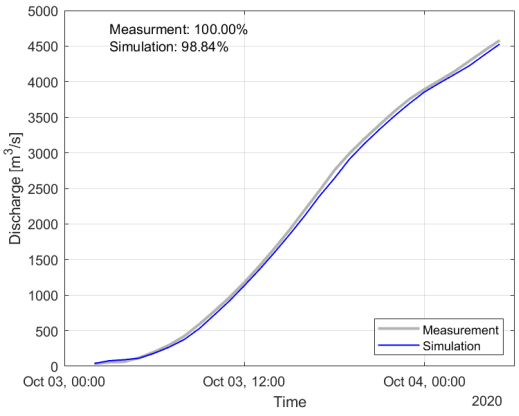

(d) Inn-Martina: cumulative flow

Figure A.12: Comparison of simulated and measured flow (BAFU) at Inn-Tarasp and Inn-Martina using HF1 for calibration

Table A.1: Calibrated K_s values ($m^{1/3}/s$) along study Inn river

Distance range (km)	K_s ($m^{1/3}/s$)	Distance range (km)	K_s ($m^{1/3}/s$)
0–1.44	30	1.44–3.06	33
3.06–6.15	33	6.15–9.107	35
9.107–14.684	30	14.684–16.832	37
16.832–24.8	30	24.8–26.138	33
26.138–31.761	30	31.761–39.44	33
39.44–54.704	35	54.704–58.051	37

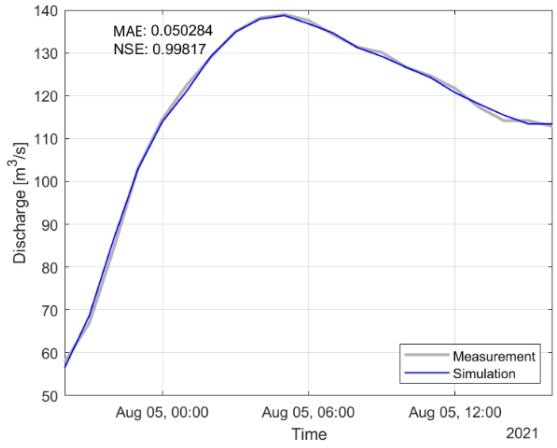

(a) Inn-Tarasp: continuous flow

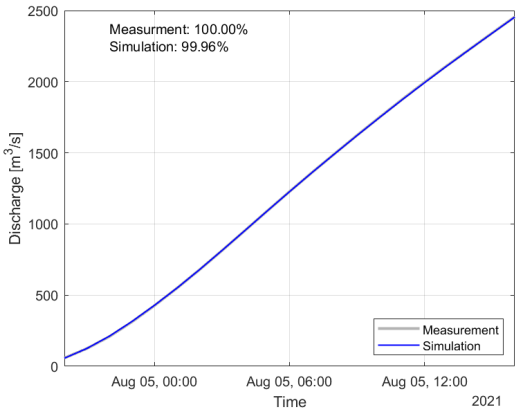

(b) Inn-Tarasp: cumulative flow

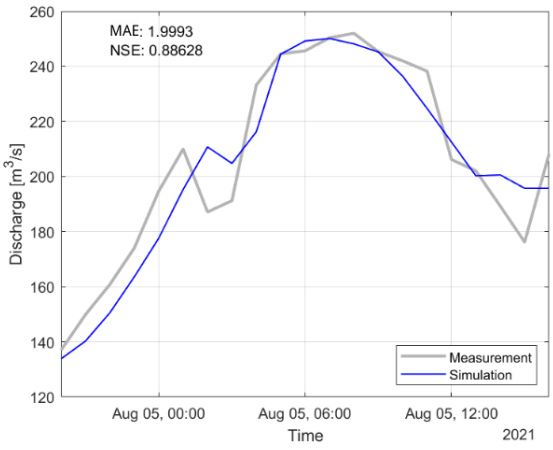

(c) Inn-Martina: continuous flow

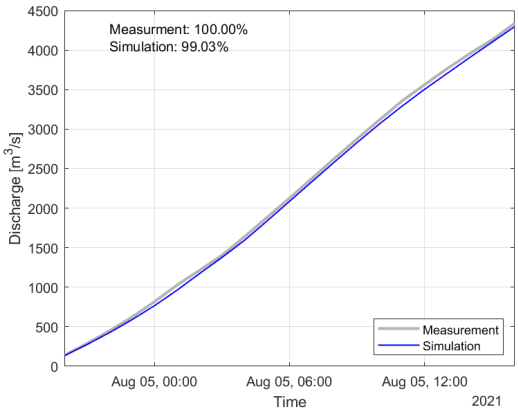

(d) Inn-Martina: cumulative flow

Figure A.13: Comparison of simulated and measured flow (BAFU) at Inn-Tarasp and Inn-Martina using HF2 for validation

Based on Table A.1, the Strickler coefficients (K_s) of the studied river reach reaches an average value of 33 $m^{1/3}/s$ with range from 30 - 37 $m^{1/3}/s$, indicating moderate roughness. Looking into the model validation results based on HF2 in Figure A.13, the overall performance is satisfactory, with only a slight tendency for underestimation. However, the model performs better at Tarasp compared to Martina. Figure A.13c reveals a noticeable delay in the simulated results at the

beginning of the event and a failure to capture the declining discharge at the event's end. The possible reason could be the inaccurate estimation of EKW-Martina location in the studied river reach, considering that the discharge time series at Martina is significantly influenced by the EKW-Martina data.

A.11 Formulas for Froude number and Mean Flow Depth

The Froude number (F) for open channel flow is calculated as:

$$F = \frac{U}{\sqrt{gR_h}} \tag{A.10}$$

where

- U = flow velocity (m/s),
- g = gravitational acceleration (m/s^2),
- R = hydraulic radius (m), calculated as $R_h = \frac{A}{P}$, where A is the cross-sectional flow area (m^2) and P is the wetted perimeter (m).

The mean flow depth h, expressed in meters (m), is the average vertical distance from the water surface to the riverbed and is calculated as:

$$h = \frac{\Omega}{w} \tag{A.11}$$

where:

- Ω = wetted area (m^2).
- w = water surface width (m), defined as the horizontal distance across the water surface at the cross section.

A.12 Determination of Correction Factor γ

1. RESIDUAL Mass Conservation:

$$R_1 = \left[\frac{\left(\sum_i^N U_i \Omega_i - Q \right)}{Q} \right]^2 \tag{A.12}$$

2. RESIDUAL Energy averaging:

$$R_2 = \left[\frac{\left(\frac{\sum_i^N U_i^3 \Omega_i}{U^2 Q} - \alpha \right)}{\alpha} \right]^2 \tag{A.13}$$

Minimization Algorithm: To determine the optimal value of the correction factor γ, the squared residuals R_1 and R_2 were minimized with respect to γ, where $U_i = \gamma U_{i,\mathrm{NF}}$. Specifically,

squaring the residuals ensured that all error contributions were taken into account, regardless of sign, and placed greater weight on larger discrepancies. This approach enhanced the robustness of the minimization procedure by increasing its sensitivity to outliers and facilitated the convergence of the optimization algorithm. As a result, the value γ was identified.

A.13 Formulas for Bedload Transport Calculation

A.13.1 Uniform Grain Size Distribution

Meyer-Peter and Müller (1948)

$$\Phi = 8(\Theta - \Theta_c)^{3/2}$$

where $\Theta_c^{=}0.047$.

Parker (1979)

Parker proposed the following bedload transport equation for a straight gravel-bed river:

$$\Phi = 11.2\frac{(\Theta - 0.03)^{9/2}}{\Theta^3}$$

Parker et al. (1982)

$$W^* = \begin{cases} 11.2\left(1 - \frac{0.822}{\phi_{50}}\right)^{4.5} & \text{if } \phi_{50} > 1.65 \\ 0.0025\exp\left[14.2(\phi_{50} - 1) - 9.28(\phi_{50} - 1)^2\right] & \text{if } 0.95 \leq \phi_{50} \leq 1.65 \\ 0.0025\phi_{50}^{14.2} & \text{if } \phi_{50} < 0.95 \end{cases}$$

where

$$\phi_{50} = \frac{\tau_{50}^*}{\tau_{r50}^*}; \quad \tau_{50}^* = \frac{\tau}{\rho\Delta g d_{50}}; \quad \tau_{r50}^* = 0.0876$$

Rickenmann (1991)

$$\Phi = \frac{3.1}{(i_b - 1)^{0.5}}\left(\frac{d_{90}}{d_{30}}\right)^{0.2}\Theta^{0.5}\left(\Theta - \Theta_c\right)\,\mathrm{Fr}^{1.1}$$

where $\Theta_c = 0.05$.

Wong and Parker (2006)

$$\Phi = 4.93(\Theta - \Theta_c)^{1.6}$$

where $\Theta_c = 0.047$

Recking (2013)

$$\Phi = \frac{14\Theta^{2.5}}{1+\left(\frac{\Theta_c}{\Theta}\right)^4} \quad \text{with} \quad \Theta_c = (5i_b + 0.06)\left(\frac{d_{84}}{d_{50}}\right)^{4.4}\sqrt{i_b} - 1.5$$

A.13.2 Mixing Grain Size Distribution

Parker (1990)

The Parker (1990) equation is designed for gravel-bed rivers. Therefore, the sand fraction (d 2 mm) was excluded from calculation. The gravel was divided into N size ranges, $j = 1, \ldots, N$, each with a geometric mean diameter d_j and fractional content of F_j. The gravel size fractions were defined using increments on the $1 - \varphi$ scale, where $\varphi = -\log_2(d)$ with d being the particle diameter in millimeters.

$$W_j^* = \begin{cases} 11.9\left(1 - \frac{0.853}{\phi}\right)^{4.5} & \text{if } \phi_{50} > 1.59 \\ 0.00218\exp\left[14.2(\phi-1) - 9.28(\phi-1)^2\right] & \text{if } 1.0 \leq \phi_{50} \leq 1.59 \\ 0.00218\phi^{14.2} & \text{if } \phi_{50} < 1.0 \end{cases}$$

where

$$\phi = 1.048\phi_{50}\left(\frac{d_j}{d_{50}}\right)^{-0.0951}$$

Wilcock and Crowe (2003)

Wilcock and Crowe (2003) proposed a bedload transport equation in sand- and gravel-bed rivers.

$$W_j^* = \begin{cases} 0.002\varphi^{7.5} & \text{for } \varphi < 1.35 \\ 14\left(1 - \frac{0.894}{\varphi^{0.5}}\right)^{4.5} & \text{for } \varphi \geq 1.35 \end{cases}$$

where

$$\varphi = \tau/\tau_{rj}$$

with

$$\frac{\tau_{rj}}{\tau_{rm}} = \left(\frac{d_j}{d_{sm}}\right)^b$$

$$b = \frac{0.67}{1+\exp\left(1.5 - \frac{d_j}{d_{sm}}\right)}$$

and

$$\tau_{rm} = \tau_*\Delta\rho g d_{sm}$$

$$\tau_* = 0.021 + 0.015\exp(-20F_s)$$

A.13.3 Conversion of Dimensionless to Dimensional Bedload Transport Rate

The dimensionless bedload transport rates, Φ and W^*, were converted to the dimensional bedload transport rate (Q_b) for further analysis. For the dimensionless rate Φ, Equation A.14 was employed:

$$\Phi = \frac{Q_b}{W\sqrt{g\Delta d_s^3}} \tag{A.14}$$

where Q_b is the volumetric bedload transport rate (m^3/s), W is analyzed width of the channel (m), g is the gravitational acceleration (m/s^2), $\Delta = (\rho_s/\rho - 1)$ is the submerged specific gravity of sediments, and d_s is the characteristic grain size. For most formulas d_{50} was used for d_s, except for the Recking (2013) formula where d_{84} was used.

Parker et al. (1982) introduced another dimensionless bedload transport rate, W^*, defined as:

$$W^* = \frac{\Delta g Q_b}{u_*^3} \tag{A.15}$$

where u_* is the shear velocity.

To account for mixtures of grain sizes and the associated hiding effects in bedload transport, the formulas by Parker Parker (1990) and Wilcock Wilcock and Crowe (2003) were utilized. The dimensionless bedload transport rate for each grain size fraction (j) is defined as W_j^*:

$$W_j^* = \frac{\Delta g Q_{bj}}{F_j u_*^3 W} \tag{A.16}$$

where Q_{bj} is the volumetric transport rate for size fraction j, F_j is the proportion of grain size class j in the surface bed material.

For the analysis, bedload sediments were first separated into N size fractions. The transport rate for each fraction (Q_{bj}) was calculated using the respective transport formula, and the total bedload transport rate (Q_b) was then obtained by summing over all size fractions:

$$Q_b = \sum_{j=1}^{N} Q_{bj} \tag{A.17}$$

Eidgenössische Technische Hochschule Zürich
Swiss Federal Institute of Technology Zurich

Declaration of originality

The signed declaration of originality is a component of every written paper or thesis authored during the course of studies. **In consultation with the supervisor**, one of the following two options must be selected:

☐ I hereby declare that I authored the work in question independently, i.e. that no one helped me to author it. Suggestions from the supervisor regarding language and content are excepted. I used no generative artificial intelligence technologies[1].

☒ I hereby declare that I authored the work in question independently. In doing so I only used the authorised aids, which included suggestions from the supervisor regarding language and content and generative artificial intelligence technologies. The use of the latter and the respective source declarations proceeded in consultation with the supervisor.

Title of paper or thesis:

A Refined Morphodynamic Framework for the River Inn: Trajectories and Sediment Transport

Authored by:
If the work was compiled in a group, the names of all authors are required.

Last name(s):	**First name(s):**
He	Yang

With my signature I confirm the following:
- I have adhered to the rules set out in the Citation Guidelines.
- I have documented all methods, data and processes truthfully and fully.
- I have mentioned all persons who were significant facilitators of the work.

I am aware that the work may be screened electronically for originality.

Place, date	**Signature(s)**
Zürich 24.7.2025	何阳 Yang He

If the work was compiled in a group, the names of all authors are required. Through their signatures they vouch jointly for the entire content of the written work.

[1] For further information please consult the ETH Zurich websites, e.g. https://ethz.ch/en/the-eth-zurich/education/ai-in-education.html and https://library.ethz.ch/en/researching-and-publishing/scientific-writing-at-eth-zurich.html (subject to change).